White Rose Research Online

eprints@whiterose.ac.uk
https://eprints.whiterose.ac.uk
Universities of Leeds, Sheffield and York

Deposited via The University of York.

White Rose Research Online URL for this paper:
https://eprints.whiterose.ac.uk/id/eprint/246252/

Version: Accepted Version

Article:
Cho, Y., Kim, Y. H., Navin, A. et al. (2026) Evolution of high-spin states in neutron-rich 195--202Au isotopes approaching the N=126 shell closure. Physical review. C. 034313. ISSN: 2469-9993

https://doi.org/10.1103/nclr-tjv1

Reuse
This article is distributed under the terms of the Creative Commons Attribution (CC BY) licence. This licence allows you to distribute, remix, tweak, and build upon the work, even commercially, as long as you credit the authors for the original work. More information and the full terms of the licence here: https://creativecommons.org/licenses/

Takedown
If you consider content in White Rose Research Online to be in breach of UK law, please notify us by emailing eprints@whiterose.ac.uk including the URL of the record and the reason for the withdrawal request.

UNIVERSITY OF LEEDS
University of Sheffield
UNIVERSITY of York

Evolution of high-spin states in neutron-rich $^{195-202}$Au isotopes approaching the $N = 126$ shell closure

Y. Cho [1,2,3] Y. H. Kim [3,*] A. Navin [4] M. Rejmund [4] A. Lemasson [4] D. Ramos [4] E. Clément [4] C. Yuan [5] M. Liu [5] P. van Isacker [4] A. N. Andreyev [6] J. Dudouet [7] S. Choi [1,2] Y. Son [1,2,3] A. Mukherjee [3] D. Ackermann [4] G. de Angelis [8] S. Bae [3] R. Banik [9] S. Bhattacharya,[10] S. Bhattacharyya [10] K. Chae [11] F. Didierjean [12] C. Fougéres [4] G. de France [4] G. Fremont,[4] J. Goupil,[4] G. M. Gu [11] J. Ha [13] K. I. Hahn [3] Y. Hirayama [14] S. Jeong [14] C. H. Kim [11] M. J. Kim [11] S. H. Kim [11] W. Korten [15] P. Marini [4,16] H. Miyatake [14] M. Mukai [14,17] G. Mukherjee [10] T. Niwase [14] T. Otsuka [18] J. Park [3,19] R. M. Pérez-Vidal [20] F. Recchia [21] K. Rezynkina [22] P. Schury [17] J. C. Thomas [4] D. T. Kattikat Melcom [16] I. Tsekhanovich [16] A. Utepov [4] and Y. X. Watanabe [14]

[1] *Department of Physics and Astronomy, Seoul National University, Seoul 08826, Republic of Korea*
[2] *Institute for Nuclear and Particle Astrophysics, Seoul National University, Seoul 08826, Republic of Korea*
[3] *Center for Exotic Nuclear Studies, Institute for Basic Science, Daejeon 34126, Republic of Korea*
[4] *Grand Accélérateur National d'Ions Lourds, CEA/DRF-CNRS/IN2P3, Boulevard Henri Becquerel, F-14076 Caen, France*
[5] *Sino-French Institute of Nuclear Engineering and Technology, Sun Yat-Sen University, Zhuhai, Guangdong 519082, China*
[6] *School of Physics, Engineering and Technology, University of York, Heslington, York, North Yorkshire YO10 5DD, United Kingdom*
[7] *Université Lyon, Université Claude Bernard Lyon 1, CNRS/IN2P3, IP2I Lyon, UMR 5822, F-69622 Villeurbanne, France*
[8] *INFN Laboratori Nazionali di Legnaro, IT-35020 Legnaro, Italy*
[9] *Institute of Engineering & Management, Kolkata 700091, India*
[10] *Variable Energy Cyclotron Centre, 1/AF, Bidhannagar, Kolkata, West Bengal 700064, India*
[11] *Department of Physics, Sungkyunkwan University, Suwon 16419, Korea*
[12] *University of Strasbourg, CNRS/IPHC UMR7178, F-67000 Strasbourg, France*
[13] *Dipartimento di Fisica e Astronomia, Università degli Studi di Padova, Via Marzolo 8, Padova, I-35131, Italy*
[14] *Wako Nuclear Science Center, IPNS, High Energy Accelerator Research Organization (KEK), Wako, Saitama 351-0198, Japan*
[15] *CEA/DRF/IRFU, 17 rue des Martyrs 38054 Grenoble Cedex 9 France*
[16] *LP2I Bordeaux, UMR5797, Université de Bordeaux, CNRS, F-33170, Gradignan, France*
[17] *RIKEN Nishina Center, 2-1 Hirosawa, Wako, Saitama 351-0198, Japan*
[18] *Department of Physics, University of Tokyo, Hongo, Bunkyo-ku, Tokyo 113-0033, Japan*
[19] *Department of Physics, Hope College, Michigan 49423, United States*
[20] *Instituto de Física Corpuscular, CSIC-Universidad de Valencia, Valencia E-46980, Spain*
[21] *University of Padua, Via 8 Febbraio, 1848, 2, 35122 Padua, Italy*
[22] *Istituto Nazionale di Fisica Nucleare, Sezione di Padova, I-35131 Padova, Italy*

(Dated: July 26, 2026)

Background: The nuclear structure in the region southwest of the doubly magic ^{208}Pb is important to benchmark theoretical models relevant for neutron-rich heavy element formation and for the origin of the $A \sim 195$ peak in the mass abundance distribution. Although neutron-rich Pb, Tl, and Hg ($Z = 80 - 82$) isotopes are relatively well studied, experimental data for neutron-rich Au isotopes ($Z = 79$) remain largely limited due to experimental challenges.

Purpose: The purpose of this work is to investigate the evolution of the high-spin structure in neutron-rich Au isotopes near the $N = 126$ shell closure and to characterize the underlying shell-model configurations, with a particular focus on the roles of the high-j unique-parity $\pi h_{11/2}$ and $\nu i_{13/2}$ orbitals.

Methods: Neutron-rich $^{195-202}$Au isotopes were produced using multi-nucleon transfer reactions of ^{198}Pt(^{136}Xe, ^{x}I)^{y}Au at a beam energy of 7 MeV/u. Prompt and delayed γ-ray spectroscopy of isotopically identified reaction products was performed with a unique experimental setup combining the VAMOS++ large acceptance magnetic spectrometer, the AGATA HPGe γ-ray tracking array, and the CATLIFE detection system.

Results: In even-A ^{196,198,200,202}Au isotopes, prompt γ-ray transitions built on the 12^- isomer have been observed for the first time. The odd-J band built on the 11^- state vanishes for $A \geq 196$. In odd-A ^{195,197,199,201}Au isotopes, new prompt and delayed γ-ray transitions above the $11/2^-$ isomer were identified, confirming and extending the known level schemes. New isomeric states assigned to $(25/2^+)$ have been established in ^{199}Au and ^{201}Au. The minima in the excitation energies of the bands as a function of N built on the $11/2^-$ and 12^- isomers occur at ^{198}Au ($N = 119$), showing a dip against an otherwise smooth evolution.

Conclusions: Large-Scale Shell-Model calculations based on the Kuo-Herling hole effective interaction show an overall good agreement with experimental level schemes. However, the present calculations do not reproduce the minima in excitation energies at $N = 119$ observed in both Au and Hg isotopes. A systematic analysis of $\pi h_{11/2}$ and $\nu i_{13/2}$ hole occupancies, together with spin contributions of protons and neutrons, sheds light on the role of these high-j unique-parity orbitals in the generation of high-spin states. Part of the results of this work have been reported in a letter publication [1].

I. INTRODUCTION

The southwest region of the doubly-magic nucleus ^{208}Pb ($Z = 82$, $N = 126$) serves as a key testing ground for nuclear structure models for neutron-rich heavy nuclei. Spectroscopy of excited states in these rare isotopes refines our understanding of the shell structure and effective interactions used for Large-Scale Shell-Model (LSSM) calculations [2–6]. In particular, high-spin excitations, arising from a few proton holes below $Z = 82$ and neutron holes below $N = 126$, are mainly characterized by high-j unique-parity orbitals $\pi h_{11/2}$ and $\nu i_{13/2}$. These orbitals drive the systematic occurrence of long-lived isomers in odd-A (odd-even) and even-A (odd-odd) Au isotopes and shape the structure built on these isomeric states [7]. Therefore, a detailed knowledge of the level schemes above these isomers is important to elucidate the role of the high-j unique-parity orbitals in generating the high-spin structure. Furthermore, these spectroscopic data can provide valuable inputs for constraining the astrophysical r-process [8], such as theoretical predictions of (first-forbidden) β-decay rates [9–12].

The odd-A Au ($Z = 79$) isotopes, with three proton holes relative to $Z = 82$, present various structures associated with different proton single-particle configurations (See Fig. 1 of Ref. [13]). The $3/2^+$ ground state of the isotopes for $A \geq 191$ arises from the $\pi d_{3/2}$ orbital. A low-lying $11/2^-$ state involving a hole in the $\pi h_{11/2}$ orbital, often isomeric, has been observed in many of these isotopes. In even-A isotopes, the coupling of this $11/2^-$ state to a $i_{13/2}$ neutron hole produces the isomer with a spin-parity of either 11^- (for $A \leq 194$) or 12^- (for $A \geq 196$). The collective features of these structures have been interpreted using particle-plus-rotor models [14–21], and more recently, through cranking shell-model calculations that highlight the role of $\pi h_{11/2}$ and $\nu i_{13/2}$ orbitals in driving deformation as well as rotation alignment of neutron pairs [22–27]. In ^{205}Au, several levels above the $11/2^-$ isomer were well reproduced by the spherical LSSM calculations based on a three-proton hole configuration [5, 6].

Heavy-ion fusion-evaporation reactions have mainly been used to study high-spin states in neutron-deficient Au isotopes up to $A = 195$. In odd-A $^{189-195}$Au isotopes, band structures built on the $11/2^-$ isomer have been consistently identified [14–17, 22–24]. Similarly, studies of even-A $^{190-194}$Au isotopes have revealed band structures above the 11^- isomer [18, 19, 25–27]. Neutron-rich Au nuclei beyond $A = 195$ have been investigated using different methods. The $11/2^-$ isomers of ^{197}Au and ^{199}Au were studied via neutron capture reactions [28, 29] or few-nucleon transfer reactions [30]. Similarly, the $11/2^-$ isomers of ^{201}Au and ^{203}Au [31], along with the 12^- isomers of ^{196}Au [32], ^{198}Au [33], and ^{200}Au [34], have also been identified using few-nucleon transfer reactions. The β-decay study of the ground states of ^{201}Au and ^{202}Au has been performed using spallation reactions on a UCx target [35, 36]. These approaches have been currently limited to probing only the low-spin states below the isomeric states. Delayed γ-ray spectroscopy following fragmentation of a ^{208}Pb beam was used to explore high-spin states in ^{201}Au and ^{205}Au. For ^{201}Au, two γ rays cascading from the 5.6 μs isomeric state to the $11/2^-$ isomer were observed [5]. In ^{205}Au, several levels above the $11/2^-$ isomer were experimentally established [5, 6]. However, systematic studies of high-spin structures have been limited, and consequently spectroscopic data on high-spin states in neutron-rich Au isotopes near $N = 126$ remain very sparse [37].

Multi-Nucleon Transfer (MNT) reactions have revived interest as a powerful tool for producing neutron-rich nuclei near the $N = 126$ shell [38, 39]. Earlier studies have shown that the ^{136}Xe + ^{198}Pt MNT reaction is particularly effective for the population of neutron-rich nuclei in this region [40–42]. In addition, heavy-ion-induced MNT reactions are known to favor the population of high-spin yrast states [43–45]. Various nuclei in the Re-Pt region were recently studied by γ-ray spectroscopy [46–49] and laser spectroscopy [50–53] following MNT reactions. A few in-beam γ-ray spectroscopy investigations of ^{197}Au [54] and ^{195}Au [55] were carried out with high-fold γ-γ coincidence techniques. However, the difficulty in isotopic identification of MNT products has left a majority of Au isotopes with $A \geq 196$ largely unexplored. The scarce experimental data, together with improved spectroscopic capability, motivated a systematic exploration of high-spin states in neutron-rich Au isotopes via MNT reactions.

The present work reports on high-spin spectroscopy of neutron-rich Au isotopes ($^{195-202}$Au) using MNT reactions. Combining prompt-delayed γ-ray spectroscopy with isotopic identification of the reaction partners, we significantly expand our knowledge of their high-spin excited states. Several new γ-ray transitions above $11/2^-$ isomers are identified in odd-A ^{195,199,201}Au, including the half-life of new isomers in ^{199,201}Au. In even-A

* yunghee.kim@ibs.re.kr

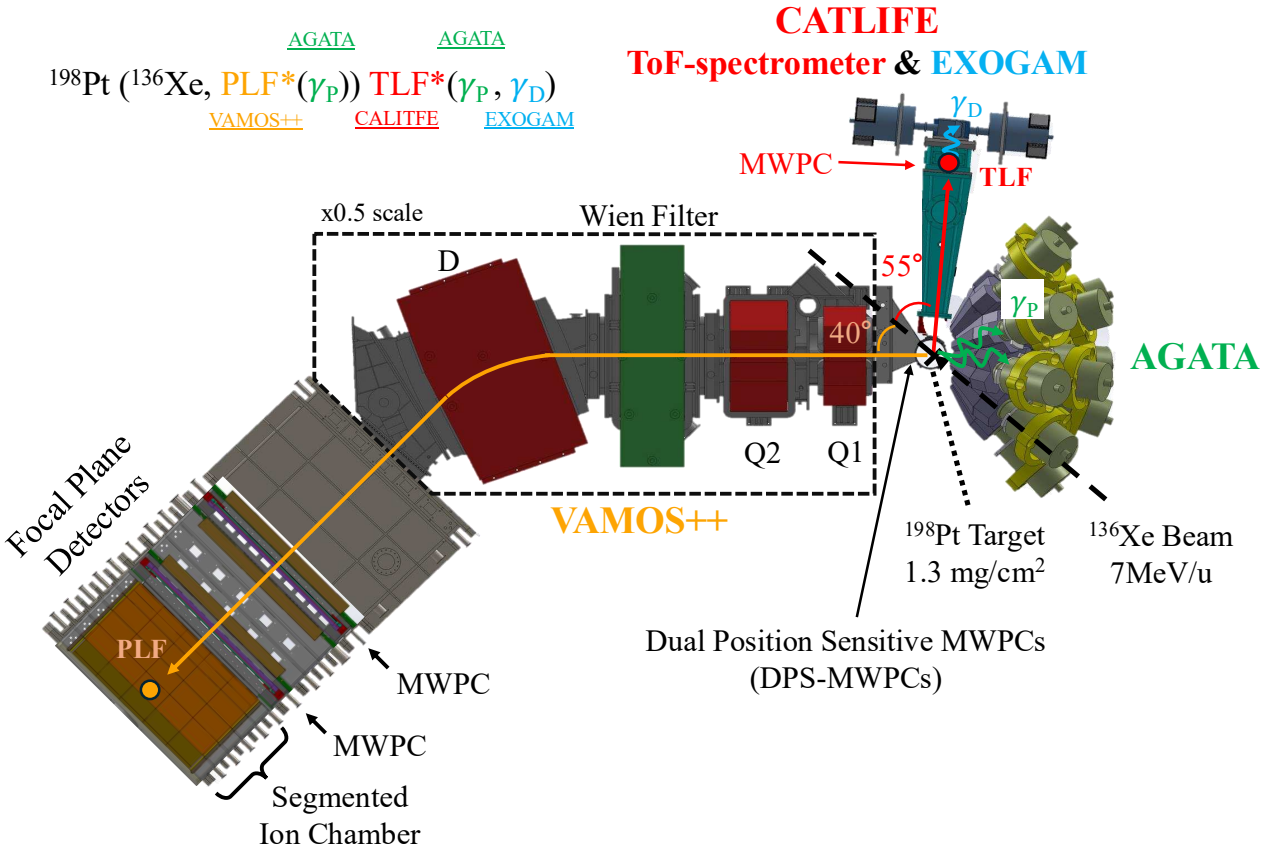


FIG. 1. Schematic top view of the experimental setup showing the various components of VAMOS++ along with the Complementary Arm for the Target-Like FragmEnts (CATLIFE) and the AGATA γ-ray detector array.

^{196,198,200,202}Au isotopes, new prompt γ-ray transitions built upon the 12^- isomers are established for the first time. The experimental level schemes are interpreted using LSSM calculations. The evolution of excitation energies for selected states in Au isotopes is discussed in the context of the corresponding states in Hg isotopes and the shell-model calculations. The hole occupancies of high-j orbitals and contributions of proton and neutron to high-spin states are systematically investigated. Part of these results have been reported in a recent related Letter [1]. The present manuscript includes new results including a comprehensive description of the experimental and theoretical analysis for the complete data for $^{195-202}$Au isotopes.

II. EXPERIMENTAL SETUP AND DATA ANALYSIS

Multi-Nucleon Transfer (MNT) reactions at energies above the Coulomb barrier were used to produce neutron-rich nuclei ranging from W to Pb in the southwest region of ^{208}Pb. A 7 MeV/u ^{136}Xe beam at the GANIL facility, with a typical beam intensity of $\sim$1.5 pnA, impinged on a 1.3 mg/cm^2-thick ^{198}Pt target [56]. Fig. 1 shows a schematic view of the experimental setup. The VAMOS++ large acceptance magnetic spectrometer [57], placed 40° near the grazing angle with respect to the beam axis, was used to detect the Projectile-Like Fragments (PLFs) produced in MNT reactions. The assembly of two Dual Position-Sensitive Multi-Wire Proportional Counters (DPS-MWPCs) [58] at the entrance of VAMOS++ provided the start signal for the time-of-flight (ToF) and the angle of the PLFs detected in VAMOS++. The detection system at the VAMOS++ focal plane included two Multi-Wire Proportional Counters (MWPCs) for ion tracking and provided the stop signal for ToF measurements. The magnetic rigidity and flight path of the ions were reconstructed from their measured positions and angles at the focal plane [59]. The suitable combinations of energy loss in an ionization chamber with seven segments were used to measure the kinetic energy and $\Delta E - E$ of the fragments. Event-by-event identification of the charge state (q), mass number (A), and atomic number (Z) of the ions was achieved by multi-parameter analysis using the measured variables [57, 59].

The distribution of q as a function of A/q is shown in Fig. 2(a). A machine learning-based calibration of the kinetic energy measurement was implemented, yielding an improvement in q resolution of about 8% [60]. Fig. 2(b) presents the $\Delta E - E$ plot for the selected mass range of $126 \leq A \leq 142$. To further improve the Z identification of the PLFs in these reactions where (quasi) elastic scattering dominates, a narrow contour around the calculated centroid for each identified Z in the $\Delta E - E$ was taken for a large number of small E bins and for each of the measured mass numbers. Fig. 2(c) illustrates the particle identification plot for the ions detected in VAMOS++. The distribution of Z is shown as a function of A for the mass range of $126 \leq A \leq 142$. The achieved resolutions are $\Delta Z/Z \simeq 1/60$, $\Delta A/A \simeq 1/210$, and $\Delta q/q \simeq 1/86$.

The Complementary Arm for Target-LIke FragmEnts (CATLIFE) [61], a newly developed detection system, was employed to aid the identification of Target-Like Fragments (TLFs). It consisted of a large MWPC and an aluminum stopper, followed by four EXOGAM HPGe Clover detectors [62] covering the area of the MWPC. The MWPC, positioned 1230 mm from the target, provided the horizontal and vertical positions of the TLFs (see Fig. 1). The time-of-flight of TLFs was determined from the time difference between the DPS-MWPC of VAMOS++ and the MWPC in CATLIFE. The latter covered a geometrical acceptance of 46.5 msr, spanning horizontal angles between 51° and 59° around the grazing of the TLFs. This coverage corresponds to about 58% of the acceptance of VAMOS++ [57]. After traversing the CATLIFE's MWPC, ions were implanted into a 2 mm-thick aluminum stopper.

Direct identification of TLFs is very challenging due to their high ($A_{\rm TLF}$, $Z_{\rm TLF}$) and low energy (< 1.5 MeV/u). Instead, the atomic number of TLFs is deduced from the identified PLF partner, assuming a binary reaction with no proton evaporation. Their mass number cannot be determined directly, since neutron evaporation can occur whenever the fragment's excitation energy exceeds the neutron separation energy. The number of neutrons emitted from a fragment has a statistical nature that depends on the excitation energy (neglecting the relatively small angular momentum dependence). Consequently, TLFs associated with a given PLF species ($A_{\rm PLF}$, $Z_{\rm PLF}$) generally comprise a mixture of several mass numbers smaller than the binary partner. In the following analysis, the excitation energy of the reaction products is treated in terms of Total Kinetic Energy Loss (TKEL) [63, 64], derived from two-body kinematics. The TKEL represents the difference in total kinetic energy between the initial system and the final fragments in the center-of-mass frame.

The four EXOGAM detectors, positioned 6 mm behind the Al stopper in CATLIFE, were used to detect γ rays emitted from the isomeric states of the TLFs. These delayed γ rays were recorded within a time window (Δt) ranging from 0.1 μs to 100 μs with respect to the DPS-MWPC of VAMOS++, which allowed half-life measurements of the isomers.

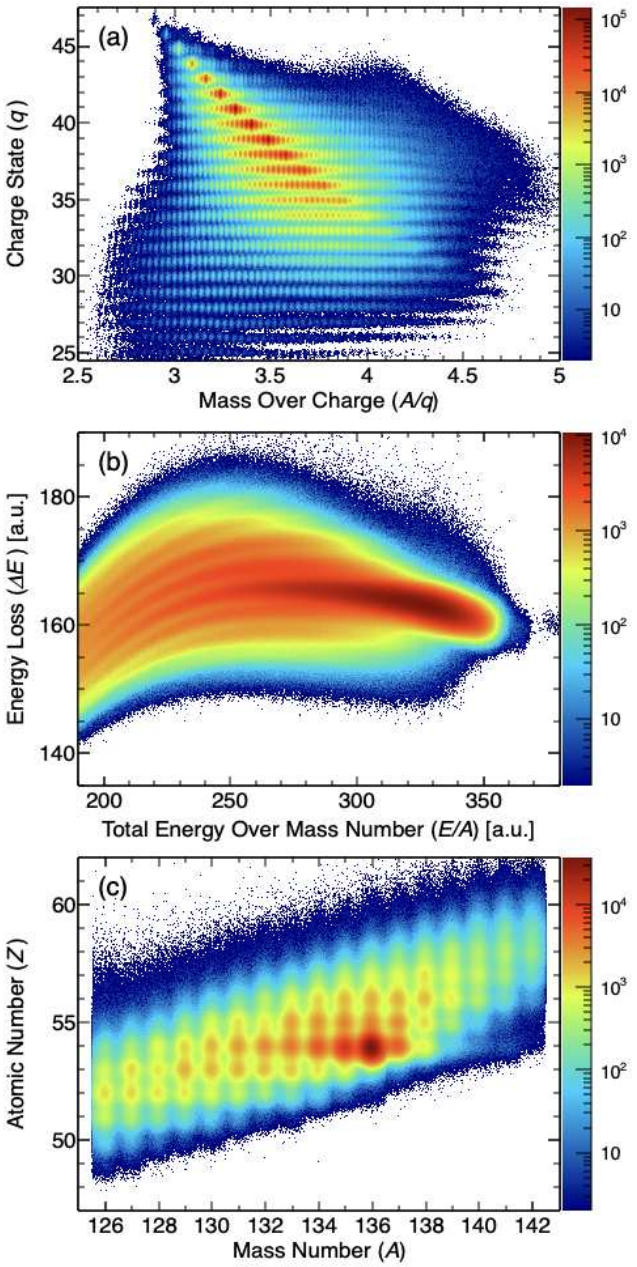


FIG. 2. Particle identification of the Projectile-Like Fragments (see text). (a) The distribution of charge state (q) as a function of mass number over charge (A/q). (b) The distribution of energy loss (ΔE) as a function of total energy over mass number (E/A) for $126 \leq A \leq 142$. (c) The distribution of atomic number (Z) as a function of mass number (A) of the ions detected by VAMOS++.

The AGATA γ-ray tracking array [65] was used to measure the prompt γ rays in coincidence with a PLF detected by the DPS-MWPC at the target position and the MWPC at the VAMOS++ focal plane. The array, comprised of 36 segmented HPGe crystals covering a solid angle of about 1π, was positioned in the backward di-

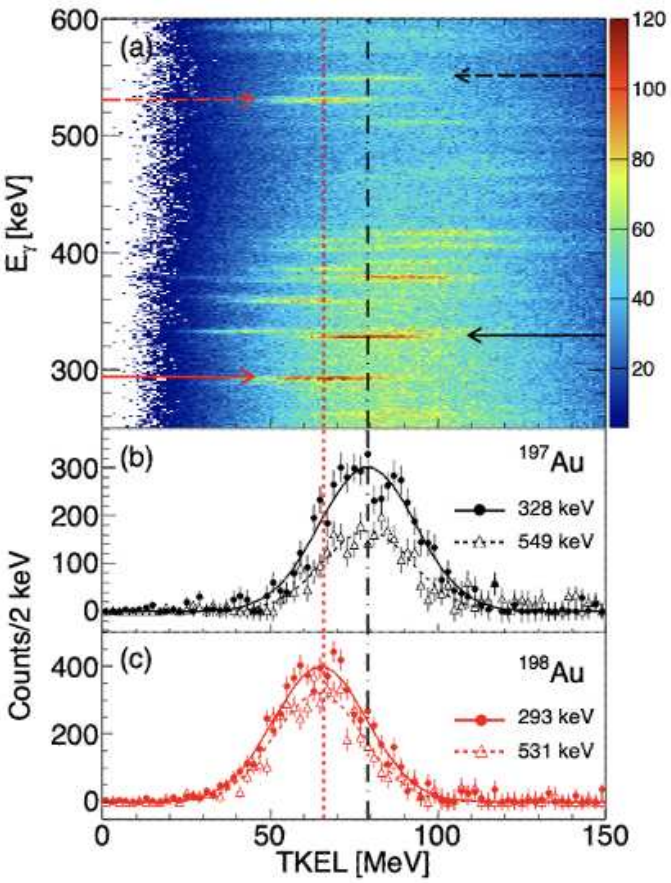


FIG. 3. (a) The Doppler-corrected prompt γ-ray spectra of the Au isotopes in coincidence with the ^{131}I partner as a function of the Total Kinetic Energy Loss (TKEL). The solid (dashed) arrows on the left and right side indicate the newly identified 293 (531) keV transition of ^{198}Au (red) and the known 328 (549) keV transitions of ^{197}Au (black), respectively. (b) The TKEL distribution for the 328 keV (filled circle) and 549 keV (open triangle) transitions of ^{197}Au. The Gaussian functions fitted for the corresponding TKEL distributions are shown as solid and dotted curves, respectively. (c) Same as (b) for 293 keV (filled circle) and 531 keV (open triangle) transitions of ^{198}Au. The Gaussian functions fitted for the corresponding TKEL distributions are shown as solid and dotted curves, respectively. The vertical red dotted and black dashed lines represent the optimal TKEL values used for the spectroscopy of the ^{198}Au and ^{197}Au, respectively (see text).

rection with respect to VAMOS++ at a distance of 235 mm (nominal configuration) [66]. A 140 ns time window was applied between the VAMOS++ trigger from DPS-MWPC and AGATA to select prompt γ-ray events.

The γ rays emitted from the isotopically selected TLFs were identified based on their correlation with the TKEL for a given PLF. The Cubix software [67], a ROOT-based program [68] developed specifically for γ-ray spectroscopy, was suitably extended and used for γ-TKEL analysis. The optimal TKEL window for a certain TLF species, associated with a specific PLF partner, was determined from the yield of its characteristic γ-ray transitions as a function of TKEL.

The Doppler correction for the prompt γ rays of the TLFs was performed using the measured velocity of their partner and the first interaction point of the γ rays in AGATA [65]. The velocity of TLFs is determined on an event-by-event basis under the assumption of a binary reaction. Uncertainties in γ-ray energies are 1 keV unless explicitly mentioned. Fig. 3(a) displays the Doppler-corrected γ-ray spectrum of Au isotopes as a function of TKEL for the case of the ^{131}I isotope as the PLF partner. The nascent binary partner of ^{131}I is ^{203}Au, assuming no neutron evaporation. The projected TKEL distributions of two known γ-ray transitions from ^{197}Au [54], the $6n$ evaporation channel, are shown in Fig. 3(b). The filled circle and open triangle histograms represent the projected TKEL distributions for the 328 and 549 keV transitions, respectively. The TKEL contributions arising from the γ-ray background were subtracted. Gaussian functions fitted to these distributions are shown as the solid line for the 328 keV transition and the dotted line for the 549 keV transition. Both transitions exhibit a common maximum near 80 MeV (marked by the vertical dashed line), which corresponds to the optimal TKEL value (<TKEL>) of ^{197}Au for a PLF partner of ^{131}I.

Fig. 3(c) presents the TKEL distributions of two newly observed γ-ray transitions at 293 keV and 531 keV, both showing maximum yields at a common TKEL value of approximately 67 MeV (marked by the vertical dotted line). Since the mean TKEL value of 67 MeV is lower than that of 80 MeV of ^{197}Au, these γ rays are emitted from a reaction channel with a lower number of neutron evaporation. No other γ-ray transitions were observed with peak yields between these two TKEL values. Thus, the 293 keV and 531 keV transitions can be assigned to ^{198}Au.

Similar analyses can be performed for the delayed γ rays using the additional correlation with the half-life of the isomeric states. The prompt and delayed γ-TKEL matrices for given iodine isotopes were systematically analyzed to identify γ-ray transitions and <TKEL> for each Au isotope. The background-subtracted TKEL distribution of each iodine isotope ($127 \leq A \leq 135$) identified in VAMOS++ is shown in Fig. 4(a). This shows a wide TKEL range for each iodine isotope, implying that several Au isotopes are generally associated with a single iodine isotope due to neutron evaporation. Fig. 4(b) illustrates the evolution of <TKEL> for the $^{195-202}$Au isotopes as a function of the iodine mass number. The error bars indicate one standard deviation of the TKEL distribution. In general, the <TKEL> of a given Au isotope increases linearly as more neutrons are transferred during the reactions (lower iodine mass number).

The $A_{\rm PLF}$, $Z_{\rm PLF}$ gated "singles" γ-ray spectra of individual Au isotopes for a given iodine isotope were obtained by projection of the γ-TKEL matrix for the optimal region around <TKEL>, typically $\pm$ 25 MeV for determining the relative transition intensities (I_γ) ($\sim \pm$

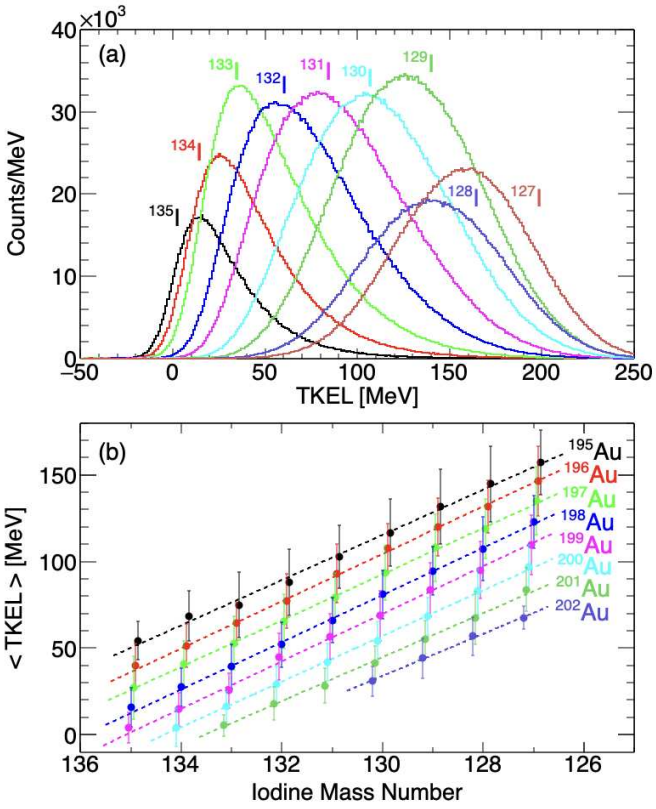


FIG. 4. (a) Total kinetic Energy Loss (TKEL) distribution for the $^{127-135}$I ($Z_{\rm PLF} = 53$) isotopes identified in VAMOS++. (b) The evolution of optimal TKEL value (<TKEL>) for each Au isotope ($195 \leq A \leq 202$) as a function of iodine mass number. The vertical bars represent the width of the TKEL distribution for each Au isotope (one standard deviation). The dashed lines are drawn to guide the eye.

15 MeV was used for generating γ-γ matrices). This approach maximizes the yield for a given Au isotope, ensuring that its characteristic γ rays dominate the spectrum. To suppress contamination from adjacent Au isotopes, γ-ray spectra from neighboring TKEL regions were appropriately subtracted. The total "singles" γ-ray spectrum focused on a single Au isotope was constructed by summing the individual "singles" spectra obtained from each iodine isotope. Relative γ-ray intensities were determined from the total "singles" γ-ray spectra. The γ-γ matrices were generated for both the prompt and delayed transitions.

III. RESULTS

A summary of the experimental level schemes of the $^{195-202}$Au isotopes obtained in the current work is presented in Fig. 5. The level schemes were built by selecting excitation energy gates using TKEL, analyzing γ-γ coincidence relationships, and γ-ray intensities. The intensities are corrected for internal conversion using BrIcc calculation [69]. Spin-parity assignments were made based on the available systematics and the Large-Scale Shell-Model (LSSM) calculations discussed in Sec. IV. A one-component exponential fit ($Ae^{-t/T}+C$, where A, T, C are the fitting parameters) was used to obtain the half-life of the isomeric states.

A. Odd-A Au Isotopes

In the odd-A isotopes ^{195,197,199,201}Au studied here, we observe a small number of transitions below the $11/2^-$ isomer and high-spin bands built upon this state. Above the $11/2^-$ isomer, additional isomeric states are identified, with half-lives ranging from a few hundred nanoseconds to several hundred microseconds.

1. ^{195}Au

Previous γ-ray spectroscopy studies for the high-spin states of ^{195}Au have been reported in Refs. [16, 24, 55]. A $(31/2^-)$ isomer with $T_{1/2} = 12.89(21)\,\mu$s was identified [55]. In the present work, we confirm the known isomeric transitions at 168, 179, 261, 388, 481, and 718 keV, as shown in the delayed "singles" γ-ray spectrum ($1 < \Delta t < 40\,\mu$s; Fig. 6(a)). The inset in Fig. 6(a) shows that a fit to the decay curve gated on the 388, 481, and 718 keV transitions results in $T_{1/2} = 12.6(8)\,\mu$s, matching the literature value. The proposed low-energy transition directly depopulating the $(31/2^-)$ isomer [55] (marked "x" in Fig. 5) was not observed in the present experiment.

Fig. 6(b) presents the "singles" Doppler-corrected prompt γ-ray spectrum (γ_P) of ^{195}Au. Seven new transitions are observed at 224, 406, 417, 655, 768, 898, and 963 keV and are shown in red. The inset in Fig. 6(b) shows a γ_P-γ_P coincidence spectrum with a sum gate on the 406 keV and 417 keV transitions, confirming their mutual coincidence. Further, as illustrated in Fig. 6(c), each of these prompt γ rays is in coincidence with the delayed γ rays that de-excite the $(31/2^-)$ isomer. On this basis, the cascade decay chain of the γ_P transitions is placed above the $(31/2^-)$ isomer. Since the 768 and 898 keV transitions have nearly equal intensities, it is possible to interchange their ordering.

Table I in the Appendix gives the details of all the transitions of ^{195}Au observed in this work.

2. ^{197}Au

The $(31/2^-)$ isomer in ^{197}Au, with a half-life of 150(5) ns, was first reported in Ref. [54]. Fig. 7(a) shows the delayed "singles" γ-ray spectrum for $80 < \Delta t < 800$ ns, in which the known isomeric transitions at 261, 358, 429, 436, and 640 keV are clearly observed. The inset in Fig. 7(a) presents the decay spectrum of the 436 keV transition, from which a half-life of 149(9) ns is extracted, in good agreement with earlier results [54]. In analogy

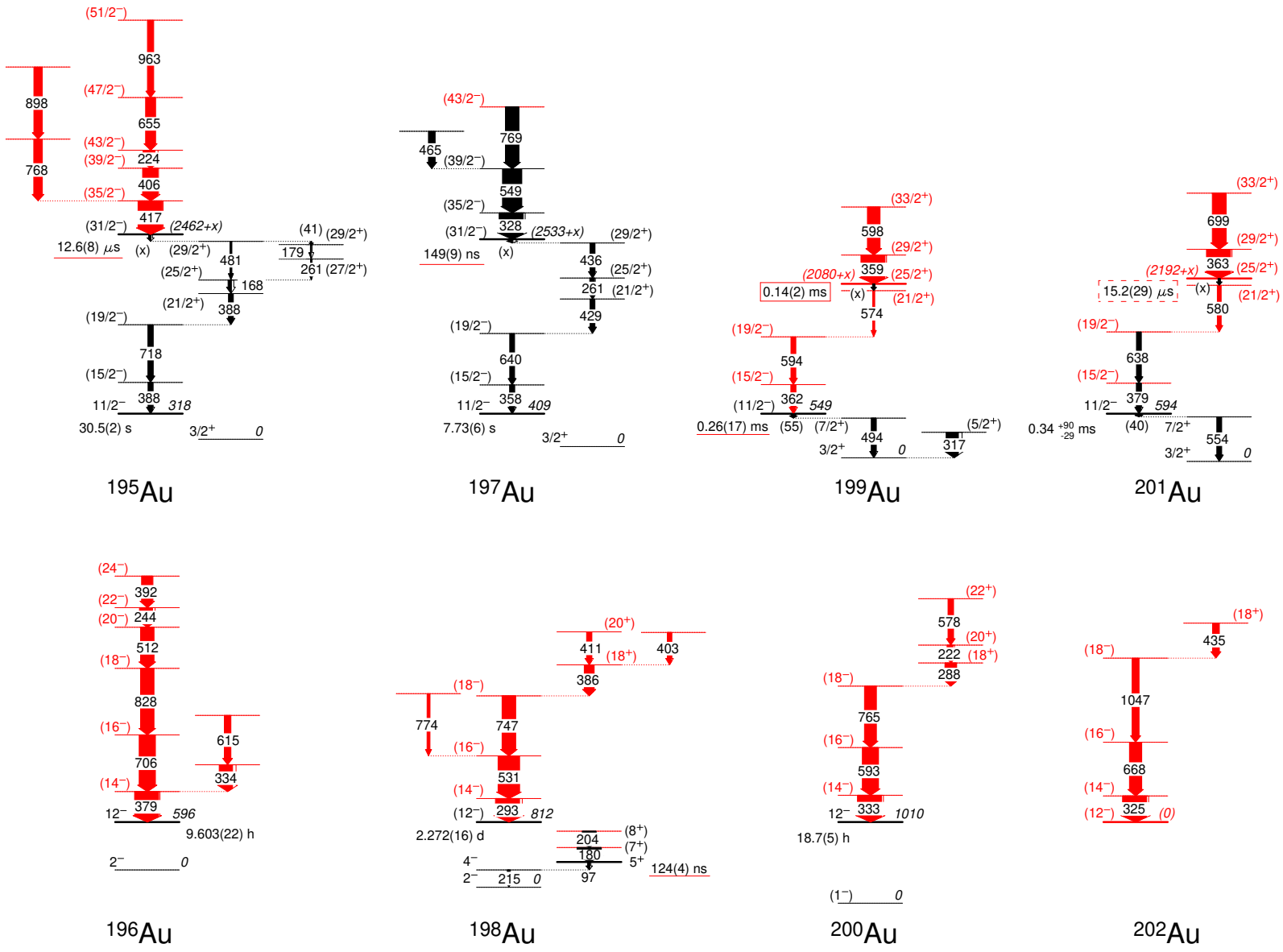


FIG. 5. The level schemes of $^{195-202}$Au isotopes obtained from the present work. The newly observed γ-ray transitions and placement of the levels are indicated in red. The thickness of the arrows indicates the intensity relative to the lowest transition of the band. Isomeric levels are highlighted with thick horizontal lines. Half-lives previously reported but remeasured here are underlined in red. Newly determined half-lives are enclosed in solid red boxes, while values in dashed red boxes indicate disagreement with earlier measurements. Half-lives not remeasured in this study are taken from Ref. [70] and are also shown. Energies of unobserved transitions are indicated in parentheses. For the even-N(odd-N) isotopes, the excitation energies are aligned with respect to the $11/2^-(12^-)$ level.

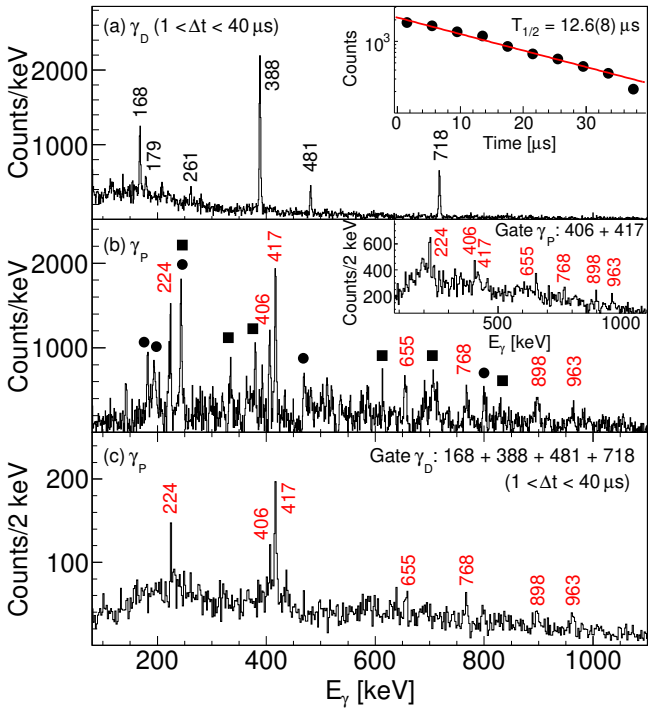


FIG. 6. γ-ray spectra for ^{195}Au obtained with gates on $^{127\text{-}135}$I within the respective optimal TKEL regions for each isotope. The new transitions are labeled in red. (a) The "singles" delayed γ-ray spectrum (γ_D) for $1 < \Delta t < 40$ μs. The inset shows the decay curve with the exponential fit (single component) with a sum gate on the three isomeric transitions (388, 481, and 718 keV). (b) The "singles" Doppler-corrected prompt γ-ray spectrum (γ_P). Transitions from ^{194}Au are marked with ● and from ^{196}Au with ■. The inset shows the γ_P-γ_P coincidence spectrum with a sum gate on the 406 and 417 keV transitions. (c) The γ_P spectrum in coincidence with a sum gate on the γ_D = 168, 388, 481, and 718 keV transitions for $1 < \Delta t < 40$ μs.

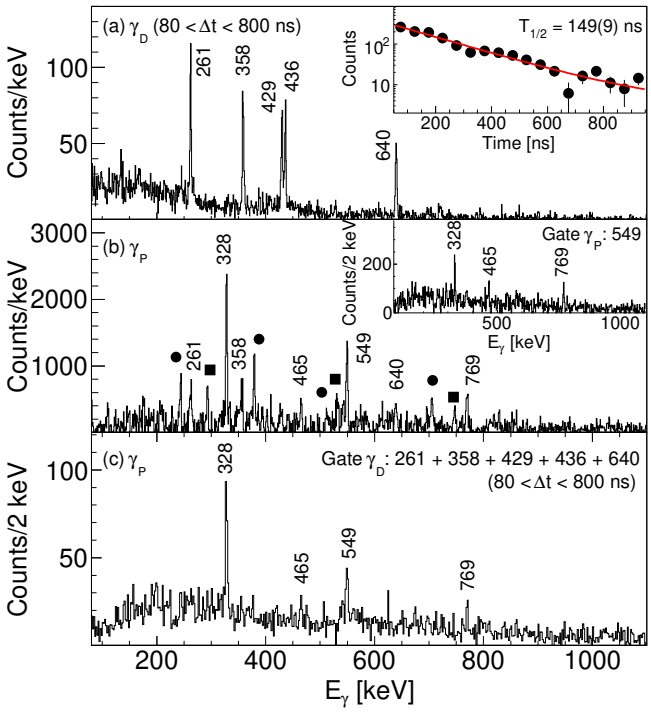


FIG. 7. γ-ray spectra for ^{197}Au obtained with gates on $^{127\text{-}135}$I within the respective optimal TKEL regions for each isotope (a) The "singles" delayed γ-ray spectrum (γ_D) for 80 $< \Delta t <$ 800 ns. The inset shows the decay curve with the exponential fit (single component) for the 436 keV isomeric transition. (b) The "singles" Doppler-corrected prompt γ-ray spectrum (γ_P). Transitions from ^{196}Au are marked with ● and from ^{198}Au with ■. The inset shows the γ_P-γ_P coincidence spectrum with a gate on the 549 keV transition. (c) The γ_P spectrum in coincidence with a sum gate on the γ_D = 261, 358, 429, 436, and 640 keV transitions for 80 $< \Delta t <$ 800 ns.

to ^{195}Au [55], the unobserved low-energy E1 transition, labeled "x" in Fig. 5, is attributed to direct decay of the $(31/2^-)$ isomer to the $(29/2^+)$ state.

In Ref. [54], several transitions above the $(31/2^-)$ isomer of ^{197}Au were also reported. Among these transitions, the 328, 465, 549, and 769 keV transitions are observed in the "singles" Doppler-corrected prompt γ-ray spectrum (γ_P) of ^{197}Au, as shown in Fig. 7(b). These prompt transitions are in coincidence with the delayed γ rays from the decay of the $(31/2^-)$ isomer (See Fig. 7(c)).

The inset in Fig. 7(b) presents the γ_P-γ_P coincidence spectrum gated on the 549 keV transition, confirming its coincidence with the 769 keV transition. This places the 769 keV transition above the 549 keV transition, in contrast to the earlier level scheme of Ref. [54], which assigns the 769 keV γ-ray as a direct feeding transition of the $(35/2^-)$ state (See Fig. 5).

Table II in the Appendix gives the details of all the transitions of ^{197}Au observed in this work.

3. ^{199}Au

The low-spin states and their decay transitions in ^{199}Au isotope were previously reported [70]. The 55 keV $M2$ transition that directly de-excites the $(11/2^-)$ isomer [71] was not detected in this experiment due to its high conversion coefficient ($\alpha_{\rm tot}$ = 283 calculated using BrIcc [69]) and low detection efficiency. However, the known 494 keV isomeric transition is observed in our "singles" delayed γ-ray spectrum (γ_D) in the time range of $1 < \Delta t < 100$ μs (See Fig. 8(a)). The extracted half-life of 0.26(17) ms (not shown in the figure) has considerable uncertainty due to low statistics and relatively long half-life, but is in agreement within the error of the literature value ($T_{1/2}$ = 0.44(3) ms) [71]. The 494 keV transition and another known transition at 317 keV [72] are also clearly observed in the "singles" Doppler-corrected prompt γ-ray spectrum (γ_P), as shown in Fig. 8(b).

The newly observed isomeric transitions at 362, 574, and 594 keV in the γ_D spectrum are shown in red in

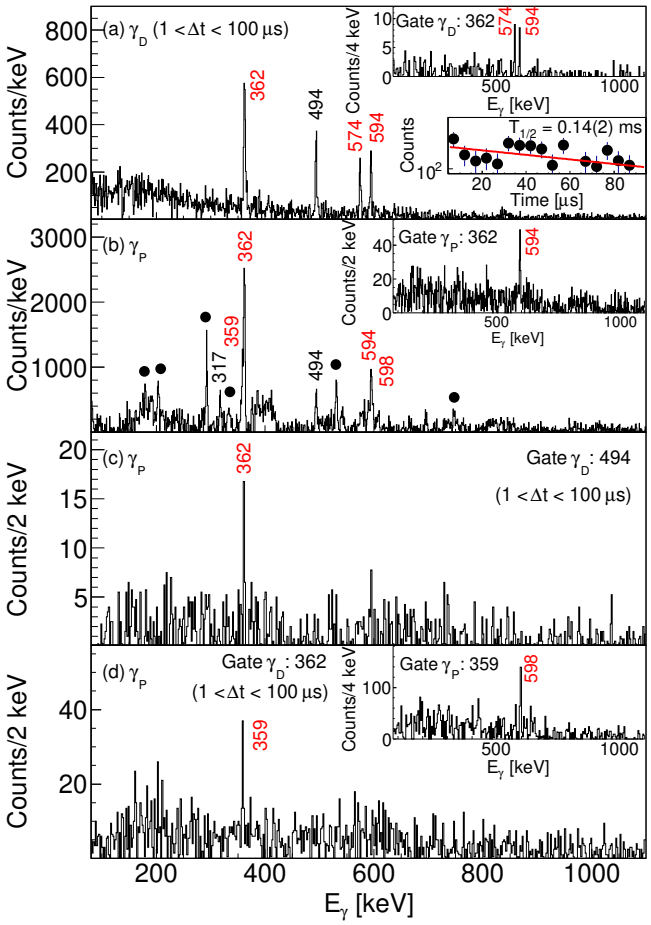


FIG. 8. γ-ray spectra for ^{199}Au obtained with gates on $^{127\text{-}135}$I within the respective optimal TKEL regions for each isotope. The new transitions are labeled in red. (a) The "singles" delayed γ-ray spectrum (γ_D) for $1 < \Delta t < 100$ μs. The upper inset shows the delayed γ-γ coincidence spectrum (γ_D-γ_D) with a gate on the 362 keV transition. The lower inset presents the decay curve along with the fit with a sum gate on the 362 and 574 keV transitions. (b) The "singles" Doppler-corrected prompt γ-ray spectrum (γ_P). Transitions from ^{198}Au are marked with ●. The inset shows the γ_P-γ_P coincidence spectrum with a gate on the 362 keV transition. (c) The γ_P spectrum in coincidence with the $\gamma_D = 494$ keV transition for $1 < \Delta t < 100$ μs. (d) The γ_P spectrum in coincidence with the $\gamma_D = 362$ keV transition for $1 < \Delta t < 100$ μs. The inset shows the Doppler-corrected γ_P-γ_P coincidence spectrum with a gate on the 359 keV transition.

Fig. 8(a). As shown in the upper inset in Fig. 8(a), these transitions are in mutual coincidence. The lower inset of Fig. 8(a) shows the decay curve with a sum gate on the 362 and 574 keV transitions. The half-life of the new isomer is determined as $T_{1/2} = 0.14(2)$ ms. The 362 and 594 keV transitions are also observed in the γ_P spectrum (Fig. 8(b)), and their coincidence is shown in the inset. In addition, the prompt 362 keV transition is in coincidence with the delayed 494 keV transition, as shown in Fig. 8(c). Therefore, a decay chain of the 362, 594, and 574 keV transitions is placed above the $(11/2^-)$ isomeric state.

In analogy to the neighboring ^{197}Au isotope, which shows a similar structure, the 574 keV transition is assumed to be an E1 decay from the $(21/2^+)$ state. The long-lived $(25/2^+)$ state is then assigned as an isomer that feeds the $(21/2^+)$ state via an unobserved low-energy E2 transition (marked "x" in Fig. 5) based on the shell-model calculations and the measured half-life. If the 574 keV transition directly depopulates the isomer, its relative intensity compared to the 362 keV and 594 keV transitions suggests a M4 character through internal-conversion analysis. However, such a high multipolarity contradicts its 0.14(2) ms lifetime and has no precedent in this mass region.

Two new prompt γ rays, 359 and 598 keV transitions, are observed in the γ_P spectrum (Fig. 8(b)). The 359 keV transition is in coincidence with the delayed 362 keV γ-ray, as shown in Fig. 8(d). The inset in Fig. 8(d) also shows the coincidence between the two prompt transitions at 359 and 598 keV. Based on these correlations, the cascade decay of the 359 and 598 keV transitions placed above the $(25/2^+)$ isomeric state.

Table III in the Appendix gives the details of all the transitions of ^{199}Au observed in this work.

4. ^{201}Au

For ^{201}Au, the earlier work reported the 554 keV transition from the decay of the $11/2^-$ isomer, with $T_{1/2} = 0.34^{+90}_{-29}$ ms, and the transitions of 379 and 638 keV from a higher-lying isomer with $T_{1/2} = 5.6(24)$ μs [5]. In the "singles" delayed γ-ray spectrum (γ_D) for the $1 < \Delta t < 100$ μs time window, all three transitions are clearly observed (See Fig. 9(a)). The 40 keV $M2$ transition that directly de-excites the $(11/2^-)$ isomer was not detected in this experiment due to its high conversion coefficient ($\alpha_{\text{tot}} = 1191$ calculated using BrIcc [69]) and low detection efficiency. A new delayed γ-ray at 580 keV is observed, which is in coincidence with the 379 keV transition (upper inset in Fig. 9(a)). The half-life obtained from the decay curve with a sum gate on the 379, 580, and 638 keV transitions is 15.2(29) μs (lower inset in Fig. 9(a)). The half-lives obtained using each transition were consistent. This value is considerably longer than the reported value of 5.6(24) μs [5].

The 379 and 638 keV transitions are also observed in the "singles" Doppler-corrected prompt γ-ray spectrum (γ_P) of ^{201}Au, as shown in Fig. 9(b). The γ_P-γ_P coincidence confirms their cascade decay (inset of Fig. 9(b)). The intensity of the prompt 379 keV transition is larger than that of the 638 keV γ-ray (See Table IV in the Appendix). Therefore, the order of the 379 keV and 638 keV transitions has been swapped, compared to the suggested decay scheme in Ref. [5].

The 580 keV transition, which is not observed in the

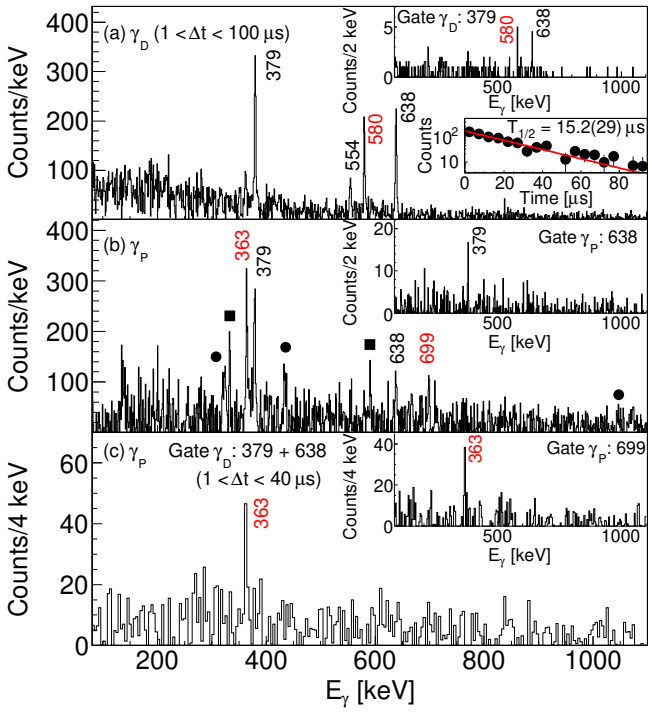


FIG. 9. γ-ray spectra for ^{201}Au obtained with gates on $^{127\text{-}135}$I within the respective optimal TKEL regions for each isotope. The new transitions are labeled in red. (a) The "singles" delayed γ-ray spectrum (γ_D) for $1 < \Delta t < 100$ μs. The upper inset shows the delayed γ-γ coincidence spectrum (γ_D-γ_D) with a gate on the 379 keV transition. The lower inset presents the decay curve along with the fit with a sum gate on delayed 379, 580, and 638 keV transitions. (b) The "singles" Doppler-corrected prompt γ-ray spectrum (γ_P). Transitions from ^{200}Au are marked with ● and from ^{202}Au with ■. The inset shows the γ_P-γ_P coincidence spectrum with a gate on the 638 keV transition. (c) The γ_P spectrum in coincidence with a sum gate on the γ_D = 379, 638 keV transitions for $1 < \Delta t < 100$ μs. The inset shows the γ_P-γ_P coincidence spectrum with a gate on the 699 keV transition.

γ_P spectrum, is placed at the top of the isomeric decay sequence. Based on analogy with the level structure of ^{199}Au, the transition is assigned as an E1 transition depopulating the $(21/2^+)$ state. Then, the $(25/2^+)$ state is proposed to be isomeric and to feed into the $(21/2^+)$ state via an unobserved low-energy E2 transition (denoted "x" in Fig. 5). If the 580 keV transition directly depopulates the isomer, its relative intensity compared to the 379 keV and 638 keV transitions would imply E2 or M2 character from internal conversion analysis. However, neither assignment is found to be compatible with the measured half-life of 15.2(29) μs.

Two new prompt γ rays at 363 and 699 keV are identified in the γ_P spectrum, as shown in Fig. 9(b). The coincidence γ_P spectrum with a sum gate on the 379 keV and 638 keV delayed transitions (Fig. 9(c)) confirms that the 363 keV transition feeds the $(25/2^+)$ isomer. The inset of Fig. 9(c) demonstrates the coincidence between the 363 keV and 699 keV transitions, placing both of them in a cascade above the $(25/2^+)$ isomer.

Table IV in the Appendix gives the details of all the transitions of ^{201}Au observed in this work.

B. Even-A Au Isotopes

High-spin states built on top of the 12^- isomer are commonly observed in the even-A ^{196,198,200,202}Au isotopes. Some previously known transitions below the isomer are also identified, while most of the observed transitions are newly established from prompt γ-ray spectra.

1. ^{196}Au

The 12^- isomer in ^{196}Au ($T_{1/2}$ = 9.603(22) h) was reported in Ref. [73]. Because of its long half-life, isomeric transitions were not observed in the current experiment. Later studies, including Ref. [74], primarily focused on low-spin excitations in this nucleus. However, most of the transitions identified in Ref. [74] were not observed in the present work, as MNT reactions predominantly populate yrast states with higher spin.

The "singles" Doppler-corrected prompt γ-ray spectrum (γ_P) for ^{196}Au is presented in Fig. 10(a). Several new transitions, 244, 334, 379, 392, 512, 615, 706, and 828 keV, have been identified. The γ_P-γ_P coincidence spectrum gated on the 379 keV transition, shown in Fig. 10(b), demonstrates coincidence among the transitions. These transitions are placed above the known 12^- isomeric state at 596 keV [32].

The coincidence γ_P spectrum gated on the 334 keV transition is shown in Fig. 10(c), where the coincidence with the 379 and 615 keV transitions are seen. In contrast, no coincidence is observed with the 706 keV transition, indicating that the 334 keV transition directly feeds the (14^-) state. A transition at 701 keV is visible, but it lacks a clear signature in the prompt "singles" spectrum and is therefore not included in the proposed level scheme.

Table V in the Appendix gives the details of all the transitions of ^{196}Au observed in this work.

2. ^{198}Au

The 5^+ isomer ($T_{1/2}$ = 124(4) ns) [75] and the (12^-) isomer ($T_{1/2}$ = 2.28(2) d) [70] of ^{198}Au were previously reported. The half-life of (12^-) isomeric state lies beyond the delayed γ-ray time window in the present work, but the 97 and 215 keV transitions de-exciting the 5^+ isomer are observed in the delayed "singles" delayed γ-ray spectrum (γ_D) for the $80 < \Delta t < 800$ ns time window (Fig. 11(a)). The obtained half-life of the 5^+ isomer is

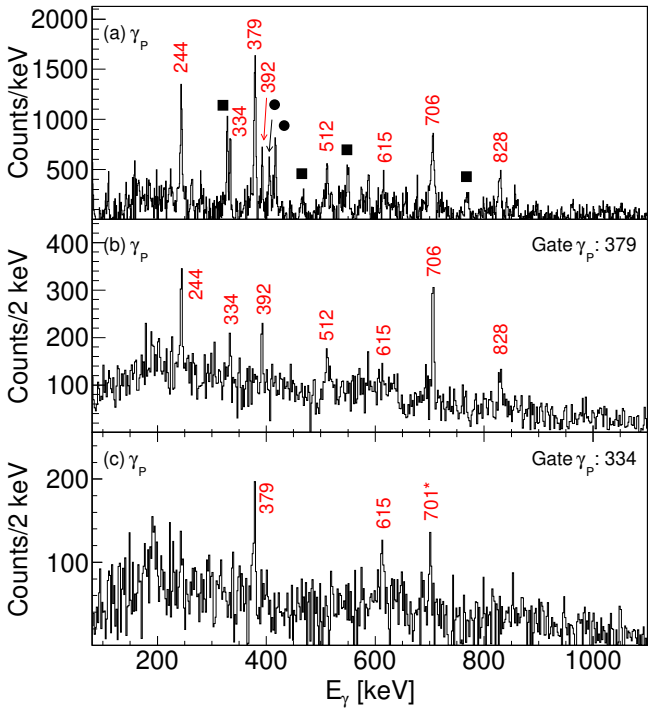


FIG. 10. γ-ray spectra for ^{196}Au obtained with gates on $^{127\text{-}135}$I within the respective optimal TKEL regions for each isotope. The new transitions are labeled in red. (a) The "singles" Doppler-corrected prompt γ-ray spectrum (γ_P). Transitions from ^{195}Au are marked with ● and from ^{197}Au with ■. (b) The γ_P-γ_P coincidence spectrum with a gate on the 379 keV transition. (c) The γ_P-γ_P coincidence spectrum with a gate on the 334 keV transition.

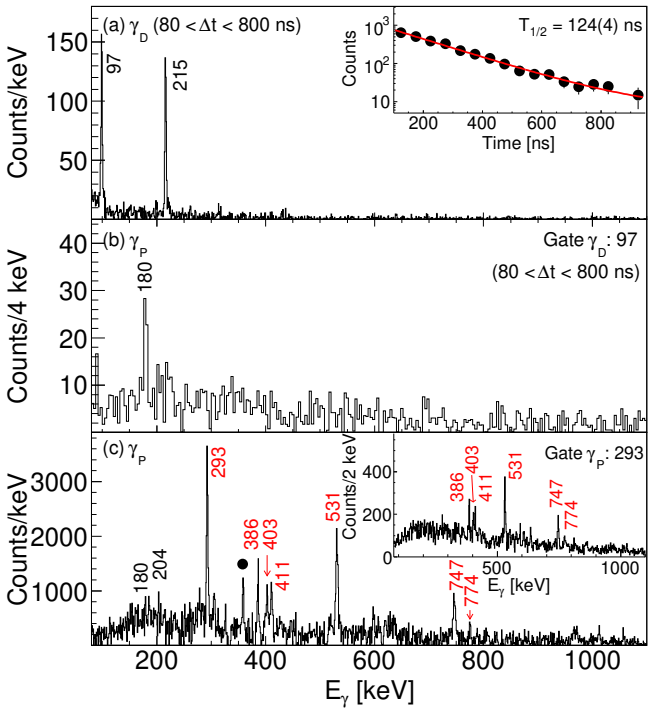


FIG. 11. γ-ray spectra for ^{198}Au obtained with gates on $^{127\text{-}135}$I within the respective optimal TKEL regions for each isotope. The new transitions are labeled in red. (a) The "singles" delayed γ-ray spectrum (γ_D) for $80 < \Delta t < 800$ ns. The inset shows the decay curve of a sum gate on the 97 and 215 keV transitions with the exponential fit. (b) The "singles" Doppler-corrected prompt γ-ray spectrum (γ_P). Transitions from ^{197}Au are marked with ●. The inset shows the γ_P-γ_P coincidence spectrum with a gate on the 293 keV transition. (c) The γ_P spectrum in coincidence with the γ_D = 97 keV transition for $80 < \Delta t < 800$ ns.

124(4) ns (inset of Fig. 11(a)), in agreement with the earlier measurement [75].

Two known 180 keV and 204 keV transitions [33] are observed in the "singles" Doppler-corrected prompt γ-ray spectrum (γ_P), as shown in Fig. 11(b). The prompt 180 keV γ-ray is also in coincidence with the delayed 97 keV transition (Fig.11(c)), confirming that it feeds the 5^+ isomer. The ordering of the 180 and 204 keV transitions, previously reported as tentative in Ref. [33], is clarified in the present work. The prompt γ-ray intensities indicate that the 180 keV transition lies below the 204 keV transition (See Table VI).

Several new prompt γ-ray transitions are identified; namely, 293, 386, 403, 411, 531, 747, and 774 keV (Fig. 11(b)). The inset in Fig. 11(c) shows the γ_P-γ_P coincidence spectrum with a gate on the 293 keV transition, which shows the mutual coincidence between the new transitions. A cascade decay of the transitions is placed above the known (12^-) state [33].

The spin-parity of the (18^+) state in ^{198}Au, which de-excites through the 386 keV transition, is tentatively assigned through a comparison with its isotone ^{199}Hg. The level scheme of ^{198}Au observed in the present work closely resembles the structure built on the $13/2^+$ state in ^{199}Hg [76]. Notably, the 386 keV transition in ^{198}Au corresponds to the 381 keV transition in ^{199}Hg, which decays from the $25/2^-$ state to the $25/2^+$ state. Given that Au isotopes can be interpreted as a proton hole in the $\pi h_{11/2}$ orbital coupled to the Hg core (See Sec. IV C), the 386 keV transition in ^{198}Au is attributed to the de-excitation of the $(18^+; h^{-1}_{11/2} \otimes 25/2^-)$ state. This systematics serves as the basis for assigning spin-parity to the corresponding states in the heavier even-A ^{200,202}Au isotopes.

Table VI in the Appendix gives the details of all the transitions of ^{198}Au observed in this work.

3. ^{200}Au

Previous γ-ray spectroscopy studies of the ^{200}Au mainly investigated low-spin excited states via β-decay spectroscopy [77, 78]. These transitions are not observed in the present measurement, which predominantly populates yrast states due to the nature of multi-nucleon

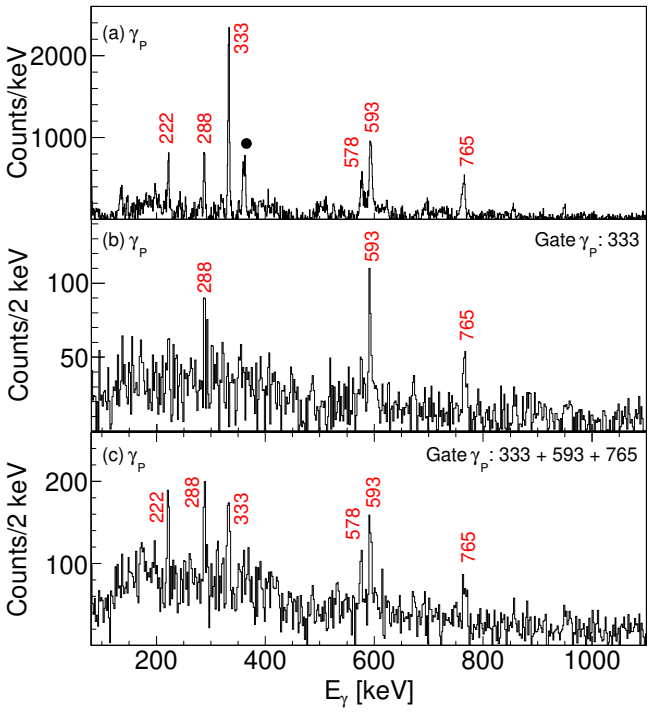


FIG. 12. γ-ray spectra for ^{200}Au obtained with gates on $^{127\text{-}135}$I within the respective optimal TKEL regions for each isotope. The new transitions are labeled in red. (a) The "singles" Doppler-corrected prompt γ-ray spectrum (γ_P). Transitions from ^{199}Au are marked with ●. (b) The γ_P-γ_P coincidence spectrum with a gate on the 333 keV transition. (c) The γ_P-γ_P coincidence spectrum with a sum gate on the 333, 593, and 765 keV transitions.

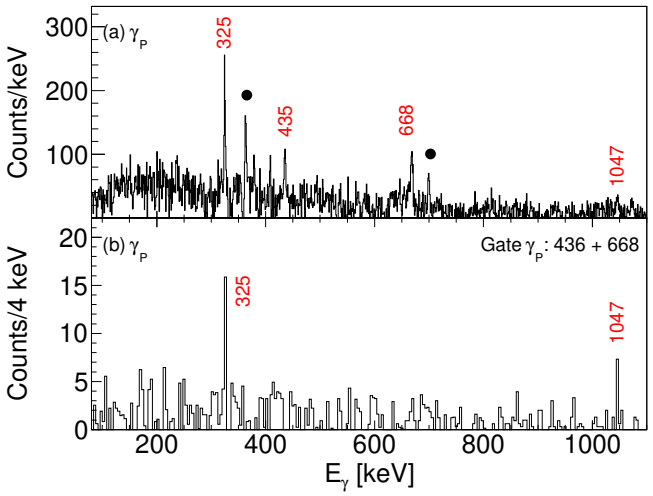


FIG. 13. γ-ray spectra for ^{202}Au obtained with gates on $^{127\text{-}135}$I within the respective optimal TKEL regions for each isotope. The new transitions are labeled in red. (a) The "singles" Doppler-corrected prompt γ-ray spectrum (γ_P). Transitions from ^{201}Au are marked with ●. (b) The γ_P-γ_P coincidence spectrum with a gate on the 325 keV transition. (c) The γ_P-γ_P coincidence spectrum with a sum gate on the 436 and 668 keV transitions.

transfer reactions [44, 45].

The "singles" Doppler-corrected prompt γ-ray spectrum (γ_P) for ^{200}Au is shown in Fig. 12(a), where newly observed transitions 222, 288, 333, 578, 593, and 765 keV are identified. The prompt γ_P-γ_P coincidence spectrum gated on the 333 keV transition confirms that the 593 and 765 keV transitions are in coincidence with the 333 keV transition (Fig. 12(b)). Therefore, the 333, 593, and 765 keV transitions are placed in a cascade above the known 12^- isomer previously reported in Ref. [77]. Additional prompt coincidence relationships among the 222, 288, and 578 keV transitions with this cascade are established from the spectrum shown in Fig. 12(c). In analogy with ^{198}Au, the state emitting the 288 keV transition is tentatively assigned a spin-parity of (18^+).

Table VII in the Appendix gives the details of all the transitions of ^{200}Au observed in this work.

4. ^{202}Au

The previous γ-ray spectroscopy study of the ^{202}Au was reported in Ref. [5]. In the present work, previously reported isomeric transitions of 138 and 414 keV [5] are not observed. These transitions were attributed to the decay of a low-lying isomer with $T_{1/2}$ = 13.1(5) ns [5], whose half-life lies outside the sensitivity of the current delayed γ-ray measurement.

The "singles" Doppler-corrected prompt γ-ray spectrum (γ_P) for ^{202}Au is presented in Fig. 13(a). Several new transitions at 325, 436, 668, and 1047 keV have been identified. The prompt γ-γ coincidence spectrum (γ_P-γ_P), gated on a sum of the 436 and 668 keV transitions, is shown in Fig. 13(b). It indicates that the 436 keV transition is in coincidence with the 325 keV transition, while the 668 keV transition is in coincidence with the 1047 keV transition. Although the coincidence between the 325 and 668 keV transitions is not clearly observed, the 668 keV γ-ray is placed above the 325 keV transition. This placement is supported by their relative intensities, the systematic trends in neighboring even-A Au isotopes, and theoretical calculations (see Fig. 16). The absence of a clear coincidence between the 325 and 668 keV transitions is likely due to the limited statistics of ^{202}Au.

Table VIII in the Appendix gives the details of all the transitions observed in this work.

C. Features of Experimental Results

The main points of the new experimental results can be summarized as follows.

1. **The appearance of a dip like structure at**

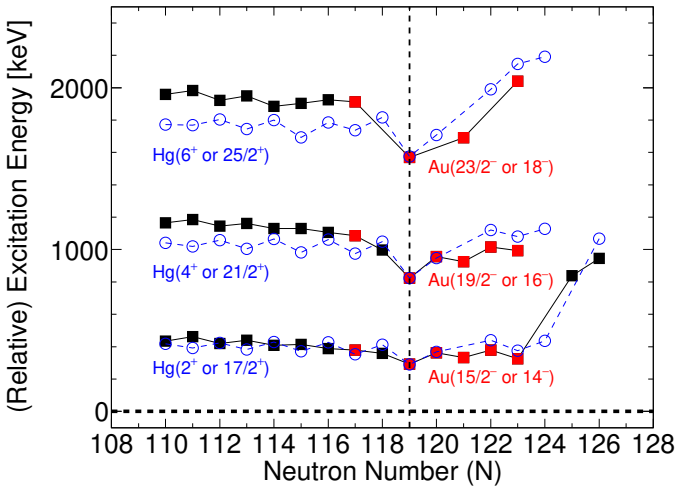


FIG. 14. Experimental excitation energies of selected $\Delta J = 2$ sequences in Au (solid black and red squares) and Hg (open blue circles) isotopes. Newly measured levels in Au ($N \geq 117$) are shown in red, while all other values are taken from Ref. [70]. Excitation energies of Au(Hg) are plotted relative to the $11/2^-(0^+)$ state for even-N and the $12^-(13/2^+)$ state for odd-N, respectively.

$N = 119$ **in the energies of low-lying states above the** $11/2^-$ **and** 12^- **isomer in the Au isotopes.**
In even-N ^{195,197,199,201}Au isotopes, negative-parity bands built on the $11/2^-$ isomer are consistently observed, while in odd-N ^{196,198,200,202}Au nuclei, analogous bands are built on the 12^- isomer. Fig. 14 shows the systematics of excitation energies for high-spin states built on the $11/2^-$ and 12^- isomer in Au isotopes. In even-N Au nuclei, members of the $\pi h_{11/2}^{-1}$ band ($15/2^-$, $19/2^-$, and $23/2^-$; black and red squares) are plotted with respect to the $11/2^-$ level. In odd-N isotopes, the $\pi h_{11/2}^{-1} \otimes \nu i_{13/2}^{-1}$ band (14^-, 16^-, and 18^-; black and red squares) is shown with respect to the 12^- state. The levels newly identified in the present work are shown in red. Up to $N = 118$, the energy spacings between successive states remain nearly constant. At $N = 119$, a drop in the level energies is observed, which becomes more pronounced at higher spin. Beyond this point, the trend recovers and then increases as the $N = 126$ shell closure is approached.

The level energy differences for Au isotopes are compared with those of the corresponding Hg nuclei in Fig. 14. Blue circles denote the energies of the even-N Hg ground-state band (2^+, 4^+, 6^+) and the odd-N $\nu i_{13/2}^{-1}$ band ($17/2^+$, $21/2^+$, $25/2^+$) with respect to the $13/2^+$ state. The excitation-energy pattern of these states in Au isotopes closely follows those of the corresponding positive-parity levels in Hg isotopes. The regularity of Au level energies and their inheritance from the corresponding Hg core are discussed in detail in Ref. [1].

2. **New** $(25/2^+)$ **isomers in the** $N > 119$ **Au isotopes.**
Newly identified long-lived isomers in ^{199}Au (0.14(2) ms) and ^{201}Au (15.2(29) μs) are tentatively attributed to the $(25/2^+)$ states, based on their delayed γ-ray spectra and prompt–delayed coincidence relationships (Figs. 8 and 9). The spectra show that only three γ-ray transitions feed the $11/2^-$ isomer, indicating a decay path $21/2^+ \rightarrow 19/2^- \rightarrow 15/2^- \rightarrow 11/2^-$. To explain the half-lives of the isomers, we invoke an unobserved low-energy E2 feeding transition into the $21/2^+$ state. For the measured half-lives, this implies a $B(E2)$ of the order of 10 W.u., comparable to the reduced transition strengths seen for the corresponding $7^- \rightarrow 5^-$ decays in neighboring Hg isotones [79]. In contrast, the positive-parity states of ^{195}Au and ^{197}Au built on the $(21/2^+)$ level end at the $(29/2^+)$ states, and the observed high-spin isomers have been tentatively assigned as $(31/2^-)$ [55]. These $(31/2^-)$ isomers likely decay to the $(29/2^+)$ state via an unobserved low-energy E1 transition [55].

3. **Non observation of the** 11^- **band in** $N > 117$ **Au isotopes.**
Previous studies of even-A ^{190,192,194}Au isotopes using fusion-evaporation reactions have revealed two band structures built on the 11^- isomer and the 12^- state [18, 25–27]. In each case, the 11^- isomer lies at a lower excitation energy than the 12^- state, and the two bands display similar level spacings with pronounced inter-band transitions linking these bands. In the present work, no clear signatures of these odd-J bands built on the 11^- state are observed for $A \geq 196$.

.

IV. SHELL-MODEL CALCULATIONS AND DISCUSSIONS

Large-Scale Shell-Model (LSSM) calculations were used to interpret the newly observed high-spin states in neutron-rich Au isotopes. The model space included five proton orbitals ($0g_{7/2}$, $1d_{5/2}$, $1d_{3/2}$, $2s_{1/2}$, $0h_{11/2}$) between the $Z = 50 - 82$ shells and six neutron orbitals ($0h_{9/2}$, $1f_{7/2}$, $1f_{5/2}$, $2p_{3/2}$, $2p_{1/2}$, $0i_{13/2}$) between the $N = 82 - 126$ shells, excluding all other orbitals. Two-body matrix elements (TBMEs) were derived from the Kuo-Herling interaction [2], with proton-proton, neutron-neutron, and proton-neutron interactions treated using the Kuo-Herling Hole Effective (KHHE) interaction framework [3]. The interaction was

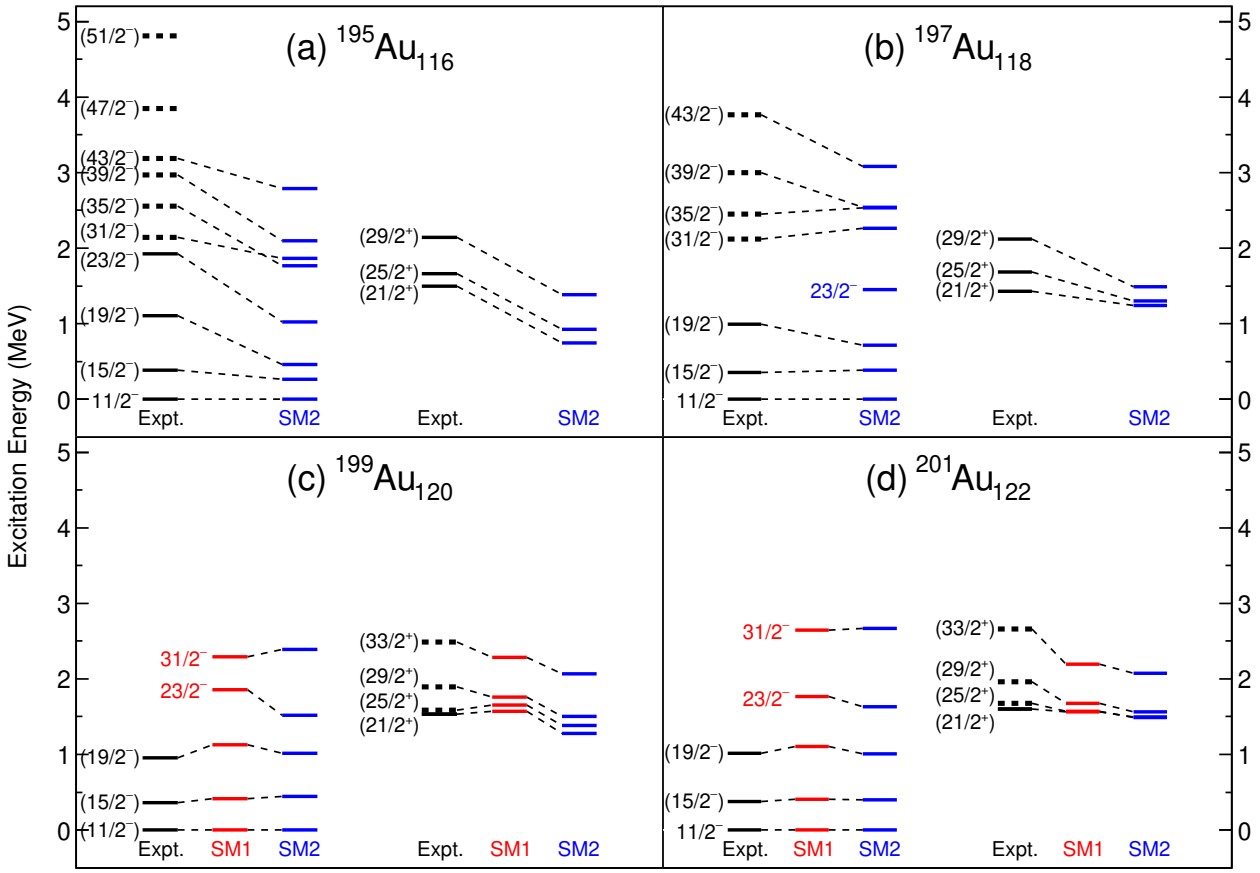


FIG. 15. Comparison of experimental (Expt., black) and shell model calculations using KHHE interaction with full model space (SM1, red) or with monopole-based truncation (SM2, blue) for level schemes of odd-A $^{195-201}$Au isotopes. The excitation energies are plotted relative to the $11/2^-$ states. Dashed levels denote that a small energy correction has been applied to account for unobserved transitions. (see Fig. 5). Experimental and shell-model states sharing the same spin–parity are connected by the dashed lines to guide the eye.

subsequently refined to improve agreement with spectroscopic data near ^{208}Pb [4]. Calculations for the $^{198-205}$Au isotopes were performed using the KSHELL code [80] within the full model space (denoted as SM1 henceforth).

As the neutron number decreases from the $N = 126$ shell closure, the computational complexity of LSSM calculations grows rapidly due to the increasing number of active single-particle configurations. To address this, the Monopole-Based Truncation (MBT) scheme [81] was applied to lighter Au isotopes ($A \leq 197$), where full model space calculations become impractical. In this approach, a subset of single-particle configurations is selected based on the sum of effective single-particle energies (E^{SC}) [81]. For the MBT calculations in the present work, configurations with $E^{SC} < 10$ MeV are retained (denoted as SM2 henceforth). This 10 MeV truncation threshold has been adopted in earlier studies and has been shown to reasonably reproduce the β-decay properties of nuclides in the southwest region of ^{208}Pb [11] and the excited-state properties in Hg isotopes [82].

A. Comparison with Level Schemes

Fig. 15 presents a comparison between experimental level schemes and shell-model predictions using the SM1 and SM2 model spaces for the odd-even $^{195-201}$Au isotopes. In particular, the calculated energies of the yrast-state are compared with the corresponding experimental data. The excitation energies are plotted relative to the $11/2^-$ isomeric state. For excited states depopulated by unobserved low-energy transitions (see Fig. 5), the level energy is tentatively assigned to be that of the feeding state, assuming the unknown low transition energies are small. The negative-parity states in ^{199}Au and ^{201}Au are well reproduced by both SM1 and SM2 calculations. However, SM2 calculations for ^{195,197}Au predict a more compressed level spacing compared to the experimental levels and the calculated results for the heavier isotopes. For positive-parity states of $^{195-201}$Au, the calculated excitation energies tend to be systematically lower than the experimental values.

Shell-model calculations show that the $21/2^+$ and $25/2^+$ states of ^{201}Au are nearly degenerate, in agree-

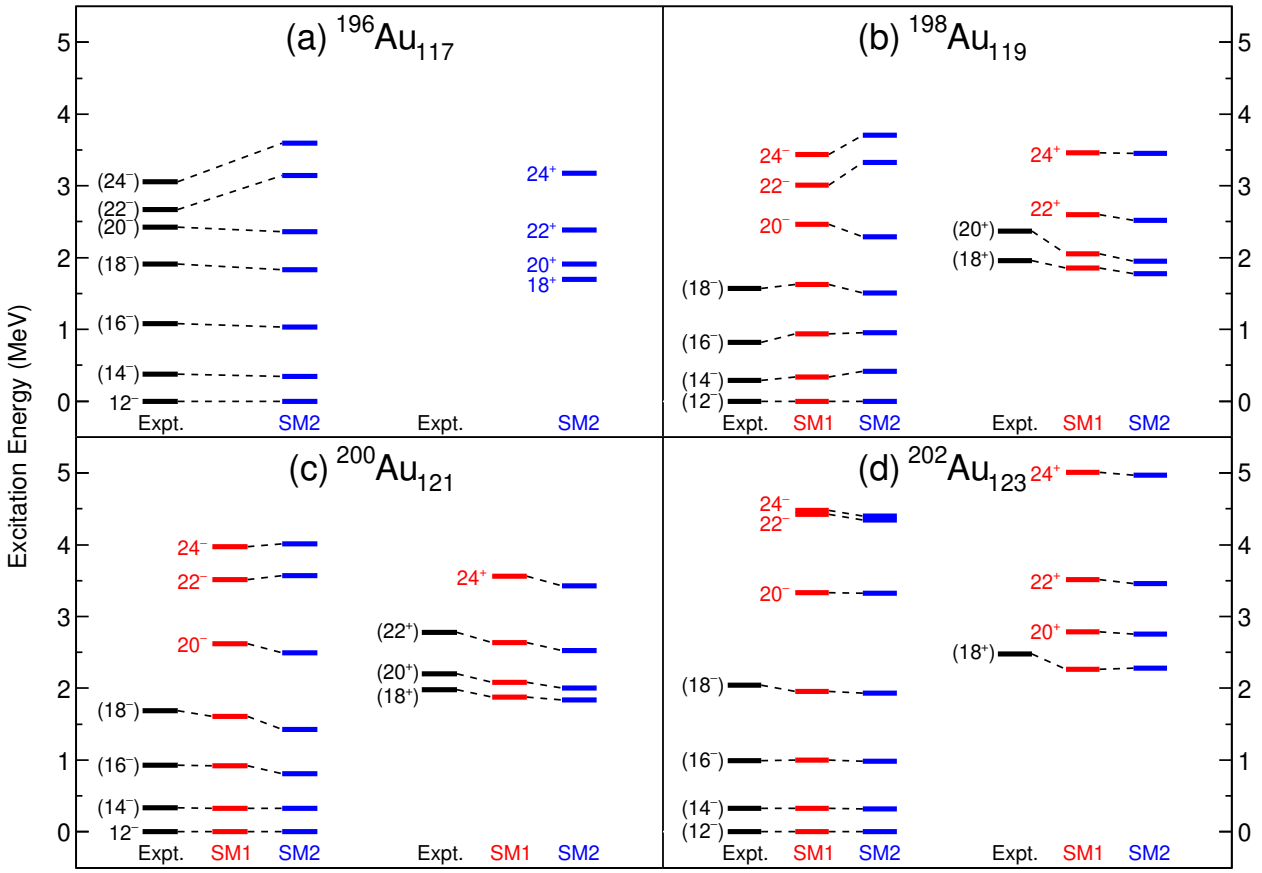


FIG. 16. Same as Fig. 15 for level schemes of even-A $^{196-202}$Au isotopes. The excitation energies are plotted relative to the 12^- states. Experimental and shell-model states sharing the same spin–parity are connected by the dashed lines to guide the eye.

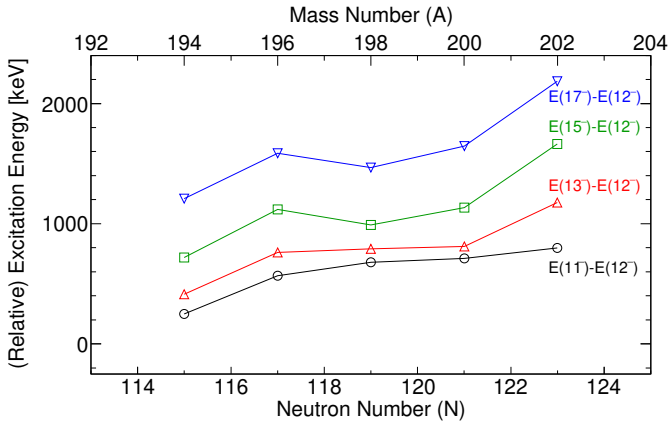


FIG. 17. The shell-model calculated excitation energies (SM2) for odd-J negative-parity states in even-A $^{194-202}$Au relative to the 12^- state.

ment with the experimental results. On the other hand, this narrow energy gap seems to be larger in the SM2 calculations for the ^{195}Au isotope, which is also in agreement with the absence of a corresponding isomer in the present work.

The experimental and calculated shell-model (SM1 and SM2 model spaces) excitation energies of odd-odd $^{196-202}$Au isotopes, relative to the 12^- isomeric state, are shown in Fig. 16. Both SM1 and SM2 shell-model calculations reproduce the observed energies relatively well, compared to those for the odd-even isotopes.

Fig. 17 shows the calculated (SM2) excitation energies of the odd-J band built on the 11^- state, plotted relative to the 12^- state, for the odd-odd isotopes $^{194-202}$Au. The excitation energies of the 11^- band relative to the 12^- state increase with the neutron number, qualitatively accounting for the lowering of the 12^- state below the 11^- state in the heavier isotopes. Consequently, inter-band transitions from even-J states to $J-1$ states are suppressed, since the $J-1$ levels lie above the J levels. This behavior was explained in terms of the variation of the neutron Fermi surface for the $\pi h_{11/2} \otimes \nu i_{13/2}$ configuration as a function of neutron number [83].

Fig. 18 shows the experimental level energies for Au isotopes along with shell-model calculations. The SM1 results (solid triangles) reproduce the overall experimental excitation energies (solid squares), but since the results are not available below $N = 119$, these calculations

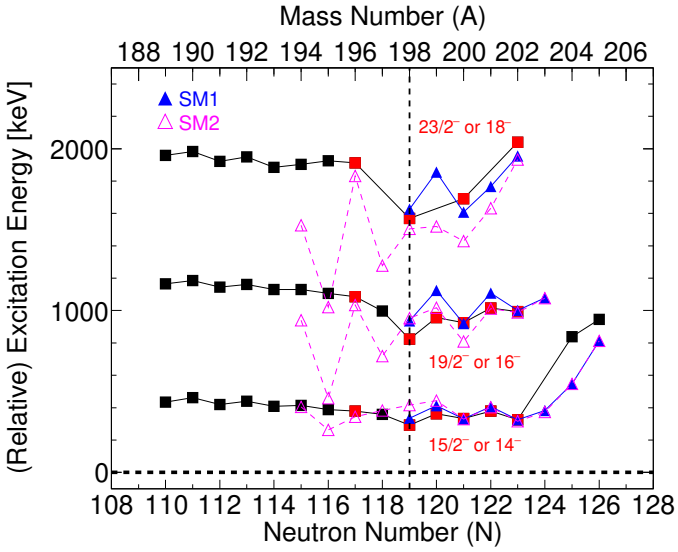


FIG. 18. Comparison of LSSM calculations with the experimental level energies of Au isotopes shown in Fig. 14. The SM1 and SM2 calculation results are denoted by solid blue and open magenta triangles, respectively. The dashed-line indicates $N = 119$, where the SM1 calculation ends.

cannot probe the energy drop at that neutron number. The SM2 calculations (open triangles) show fair agreement for even-A Au isotopes. However, the agreement is not as good for the odd-A isotopes. Therefore, the SM2 calculations that can be extended to lower-A are unable to explain the observed trend.

A notable increase of roughly 500 keV in the measured two neutron separation energy [70], $\Delta_{2n}(N) = S_{2n}(N) - S_{2n}(N+2)$, is observed at $N = 119$ for ground states in the Au isotopic chain. However, neither the binding energy differences nor the pairing energy differences for the selected levels calculated by the shell-model exhibit a minimum at $N = 119$. The underlying mechanism driving this energy drop, therefore, remains an open question.

B. $\pi h_{11/2}$ and $\nu i_{13/2}$ Hole Occupancies

To gain a deeper understanding of the high-spin states in neutron-rich Au isotopes, their underlying shell-model configurations are systematically investigated. As the neutron number decreases below $N = 126$, shell-model calculations predict that the wavefunctions in Au isotopes become more fragmented, reflecting enhanced collectivity. For example, the $11/2^-$ level in ^{205}Au ($N = 126$) is characterized by a relatively pure single-particle configuration of 73%, unlike the corresponding $11/2^-$ states in lighter isotopes ($A \leq 203$), which are highly fragmented with no single configuration contributing more than 8% to the wavefunction.

Despite pronounced fragmentation of the wavefunctions, systematic trends emerge in the hole occupancies of high-j unique-parity orbitals. Fig. 19(a) and (b) show the SM1 average hole occupancies of $\pi h_{11/2}$ and $\nu i_{13/2}$ as a function of the total spin ($2J$) for negative- and positive-parity states in odd-even $^{199-205}$Au isotopes, respectively. For the negative-parity states, the occupancy of $\pi h_{11/2}$ remains nearly one, independent of spin up to $2J = 32\,\hbar$. However, for ^{205}Au, an extra pair breaking occurs above $2J = 23\,\hbar$ (see the jump of the green solid line in Fig. 19(a)). An extra hole in the $\nu i_{13/2}$ orbital emerges at $2J = 31\,\hbar$ in ^{201}Au and ^{203}Au, and at $2J = 27\,\hbar$ in ^{199}Au. For the positive-parity states, the $\pi h_{11/2}$ and $\nu i_{13/2}$ orbitals maintain roughly one hole for these spins, with the sole exception of ^{205}Au arising from the $N = 126$ shell closure.

Fig. 19(c) illustrates the SM1 average hole occupancies in the $\pi h_{11/2}$ and $\nu i_{13/2}$ orbitals as a function of the total spin ($2J$) for negative-parity states in odd–odd $^{198-204}$Au. As in the odd–even isotopes, the $\pi h_{11/2}$ orbital carries roughly one hole for low-lying negative-parity levels. The $\nu i_{13/2}$ hole occupancy remains close to one in $^{200-204}$Au, with a slight increase in ^{198}Au. At high-spin, pair breaking in $\pi h_{11/2}$ introduces extra holes at $2J = 36\,\hbar$ in ^{204}Au, whereas $\nu i_{13/2}$ pair breaking occurs at $2J = 44\,\hbar$ in both ^{198}Au and ^{200}Au. Notably, ^{202}Au exhibits additional holes in both orbitals at $2J = 44\,\hbar$. In the positive-parity sequences shown in Fig. 19(d), the $\pi h_{11/2}$ orbital carries two holes, while $\nu i_{13/2}$ has one hole in ^{204}Au. The situation is reversed in ^{198}Au and ^{200}Au, with one hole in $\pi h_{11/2}$ and two holes in $\nu i_{13/2}$. The case of ^{202}Au exhibits a spin-dependent evolution of both $\pi h_{11/2}$ and $\nu i_{13/2}$ occupancies.

The low-lying negative-parity levels in both odd–even ($^{199-205}$Au) and odd–odd ($^{198-204}$Au) isotopes generally contain approximately one hole in the $\pi h_{11/2}$ orbital. The average hole occupancy of the $\nu i_{13/2}$ orbital tends to increase with decreasing neutron number, reflecting the increase in mixing of configurations with more than one broken pair. However, in the case of odd–odd isotopes, the low-lying negative-parity levels retain roughly one hole in the $\nu i_{13/2}$ orbital. These features are consistent with a particle–core–coupled structure in the neutron-rich Au isotopes involving high-j unique-parity orbitals, as discussed in detail in Ref. [1].

C. Proton and Neutron Spin Contributions

The spin contributions from protons and neutrons are investigated to see the respective role of protons and neutrons in the high-spin states of neutron-rich Au isotopes. Fig. 20(a) and (b) show the SM1 average spin contributions of the protons ($\langle 2J_p \rangle$) and the neutrons ($\langle 2J_n \rangle$), plotted against the total spin ($2J$) for negative- and positive-parity states in odd–even $^{199-205}$Au, respectively. In all cases except ^{205}Au, where the contribution of the proton dominates, the value of $\langle 2J_p \rangle$ remains essen-

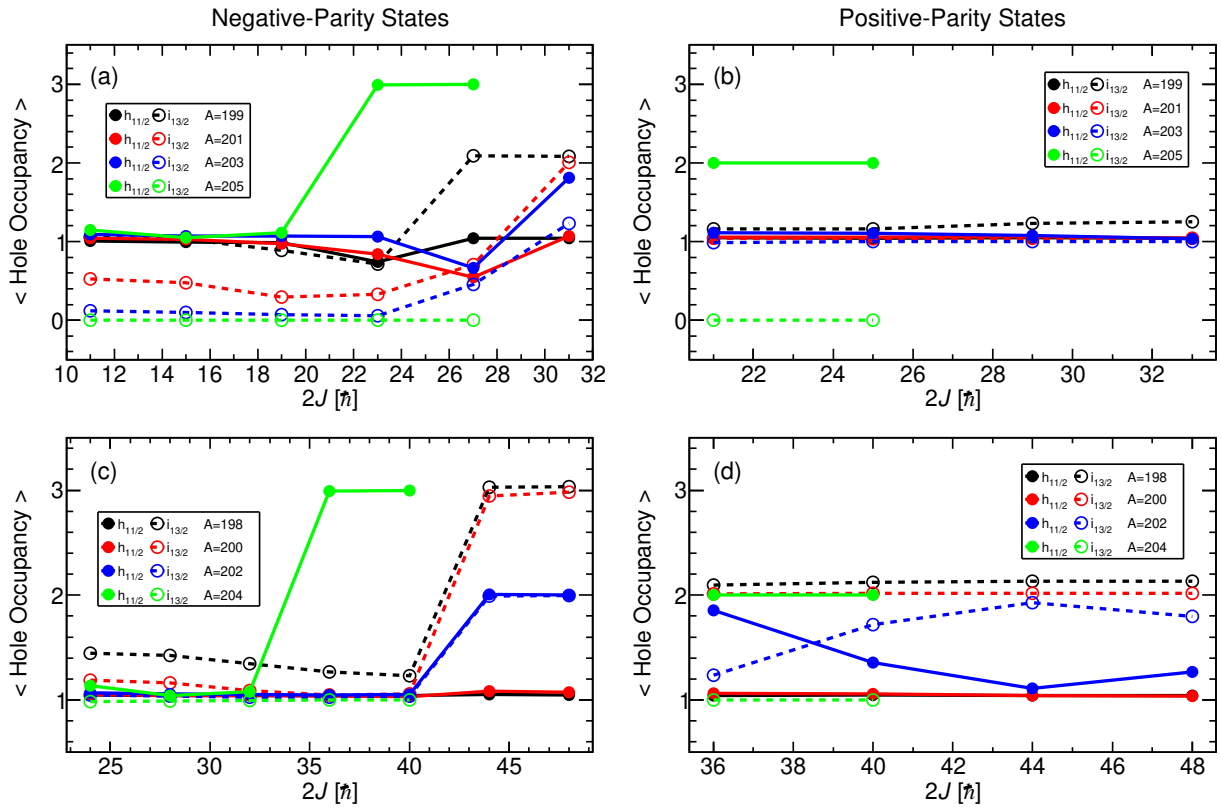


FIG. 19. (a)-(b) Shell-model calculated (SM1) average hole occupancies in the $\pi h_{11/2}$ (solid circles) and $\nu i_{13/2}$ (open circles) orbitals as a function of spin ($2J$) for negative-parity (a) and positive-parity (b) states in odd-even $^{199-205}$Au isotopes. (c)-(d) Same as (a) and (b) for odd-odd $^{198-204}$Au isotopes.

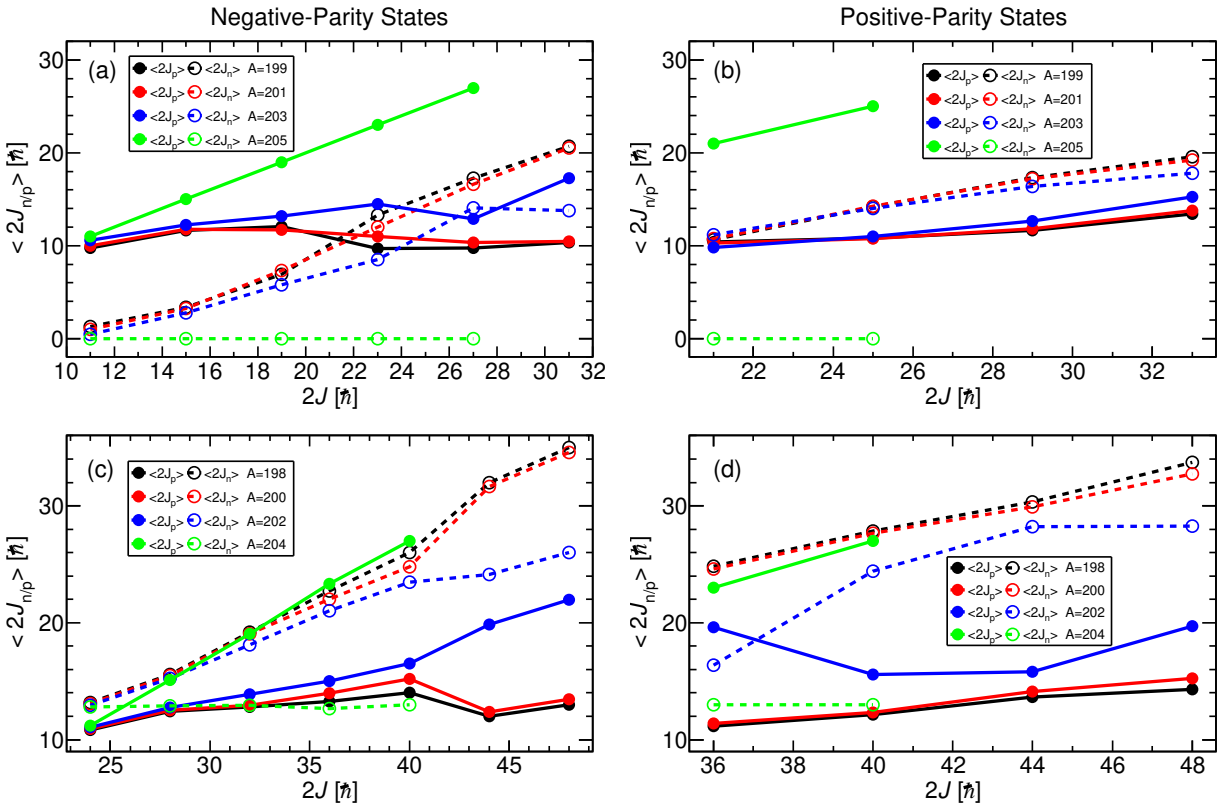


FIG. 20. (a)-(b) Shell-model calculated (SM1) neutron ($\langle 2J_n \rangle$, open circles) and proton ($\langle 2J_p \rangle$, solid circles) average spin contributions $2J_{\mathrm{n/p}}$ as a function of $2J$ for negative-parity (a) and positive-parity (b) states in odd-even $^{199-205}$Au isotopes. (c)-(d) Same as (a) and (b) for odd-odd $^{198-204}$Au isotopes.

tially constant at 11 $\hbar$. These results imply that the majority of the $\langle 2J_p \rangle$ is generated by a single $\pi h_{11/2}$ hole, although substantial mixing with the Hg core states is nevertheless present [1]. Meanwhile, $\langle 2J_n \rangle$ increases steadily as a function of spin. A similar behavior is observed in positive-parity states.

Fig. 20(c) shows the spin contributions of the negative-parity states in odd–odd $^{198–204}$Au. In ^{204}Au, $\langle 2J_n \rangle$ remains near 13 $\hbar$, corresponding to the spin carried by a single $\nu i_{13/2}$ hole. ^{198}Au and ^{200}Au show an increasing trend of $\langle 2J_n \rangle$ with spin, whereas $\langle 2J_p \rangle$ remains nearly constant, consistent with the spin contribution expected from a single $\pi h_{11/2}$ hole. In ^{202}Au, both $\langle 2J_p \rangle$ and $\langle 2J_n \rangle$ gradually increase. The positive-parity states follow a similar pattern, as shown in Fig. 20(d), except in ^{202}Au where the contributions of proton and neutron intersect at $2J = 40\,\hbar$.

In general, the average proton spin contribution exceeds that of neutrons near $N = 126$, but gradually reduces with decreasing neutron number, leading to a crossover in ^{202}Au where the neutron spin contribution becomes larger. Across these states $\langle 2J_p \rangle$ remains close to 11 $\hbar$ except for $N = 126$, whereas $\langle 2J_n \rangle$ increases steadily with total spin, underscoring the dominant role of neutrons in the building of high-spin excitations.

V. SUMMARY

Multi-nucleon transfer reactions between ^{136}Xe and ^{198}Pt at 7 MeV/u were used to access hard-to-reach neutron-rich Au isotopes in the vicinity of the $N = 126$ shell closure. The complementary capabilities of VAMOS++, AGATA, and the CATLIFE detectors enabled prompt and delayed γ-ray spectroscopy of isotopically selected Target-Like Fragments. New and extended high-spin level schemes of $^{195-202}$Au were established above the $11/2^-$ (odd-A) and 12^- (even-A) isomeric states to understand the evolution of the structure of these Au isotopes as a function of neutron number.

The $\Delta J = 2$ level sequences above the $11/2^-$ (odd-A) and 12^- (even-A) isomers are found to evolve smoothly toward the $N = 126$ shell closure. These measured level energies exhibit dips at $N = 119$ which become more pronounced in higher spin states. New $(25/2^+)$ isomers are observed in ^{199}Au and ^{201}Au, while the corresponding states are non-isomeric in lighter isotopes ($N \leq 118$). Additionally, odd-J levels built on the 11^- states seen in lighter odd-N isotopes ($N \leq 115$) are not observed in heavier isotopes ($N \geq 117$).

Shell-model calculations are in reasonable agreement with the experimental results. The calculations show the near degeneracy of the $21/2^+$ and $25/2^+$ states in ^{199}Au and ^{201}Au, supporting the experimental observations. The calculations also predict the trend of increasing the excitation energies of the 11^- band relative to the 12^- band as a function of the neutron number, explaining the missing observation of the 11^- band in $N \geq 117$. The average hole occupancies show that, for negative-parity states, a single $\pi h_{11/2}$ hole persists in both even- and odd-A nuclei, while a single $\nu i_{13/2}$ hole is maintained in the even-A isotopes. For positive-parity states in odd-A nuclei, both the $\pi h_{11/2}$ and $\nu i_{13/2}$ hole occupancies remain nearly constant for different spin states across isotopes. The relative spin contributions of protons and neutrons were also analyzed. In odd-A nuclei, the negative-parity states exhibit an almost constant proton spin contribution. In even-A nuclei, a crossover occurs at ^{202}Au. For nuclei with smaller neutron numbers, the neutron contribution becomes dominant in generating high-spin states, associated with a change in the hole occupancy of the proton $\pi h_{11/2}$ and neutron $\nu i_{13/2}$ orbitals.

The excitation energy systematics in the Au isotopes hints towards possible structural changes at $N = 119$, which is not fully reproduced by the present shell-model calculations. Interestingly, a similar feature was observed in the two neutron separation energy, $\Delta_{2n}(N) = S_{2n}(N) - S_{2n}(N+2)$, where a change of ∼500 keV appears at $N = 119$ in the ground states of the Au isotopic chains. More experimental and theoretical effort is required to understand the evolution of the level energies at $N \sim 119$.

ACKNOWLEDGMENTS

The authors are grateful for the excellent support from the GANIL accelerator staff and the AGATA collaboration. YC, YS, SC acknowledge the support from the National Research Foundation of Korea (NRF) grants funded by the Korean government (MSIT), Grants No RS-2024-00436392, RS-2022-NR070152, 2022R1A2C2005093, No. 2019K2A9A2A10017576 and No. 2020R1A2C1005981. YC, YHK, KIH, YS, JP, JH and SB acknowledge the support from the Institute for Basic Science (IBS) of the Republic of Korea (Grants No. IBS-R031-D1). AA acknowledges that the work was supported by the UK STFC and GANIL visiting researcher program. CHK, MJK, GMG, and KC were supported by the National Research Foundation of Korea (RS-2024-00338255). JH was supported by the National Research Foundation of Korea (NRF) funded by the Ministry of Education, grant. no. 2020R1A6A3A03039081. CY and ML acknowledge the National Natural Science Foundation of China under Grant No. 12475129. RPV acknowledges work partially funded by MCIN/AEI/10.13039/501100011033, Spain, with grants PID2020-118265GB-C4, PID2023-150056NB-C4, PRTR-C17.I01, by Generalitat Valenciana, Spain, with grant CIPROM/2022/54, ASFAE/2022/031, and by the EU NextGenerationEU and FEDER funds.

Appendix: Table of transition energies and intensities of $^{195-202}$Au isotopes

Summary of the observed γ-ray transitions in the studied nuclei. The energies (E_γ), relative intensities ($I_{\gamma+\mathrm{ce}}$), spin and parity of the initial (I_i) and final (I_f) states along with the level energy of the initial state (E_{level}) are presented for prompt and delayed γ rays. Intensities are corrected for detector efficiency and internal conversion calculated by BrIcc [69]. Uncertainties in γ-ray energies are 1 keV unless otherwise mentioned. Some γ-ray transitions are listed under both Prompt and Delayed, as states below the isomer can be directly populated in the reaction and their de-excitation γ rays are observed in the prompt spectrum.

TABLE I. The γ-ray transitions in ^{195}Au. The "x" denotes the unobserved low-energy transition from the $(31/2^-)$ state to the $(29/2^+)$ state.

	E_{level} (keV)	E_γ (keV)	$I_{\gamma+\mathrm{ce}}$	I_i	I_f
Prompt	x+2879	416.8	100(4)	$(35/2^-)$	$(31/2^-)$
	x+3285	406.0	63(8)	$(39/2^-)$	$(35/2^-)$
	x+3509	224.2	49(10)	$(43/2^-)$	$(39/2^-)$
	x+4164	655.4	41(5)	$(47/2^-)$	$(43/2^-)$
	x+5127	962.6	26(4)	$(51/2^-)$	$(47/2^-)$
	x+3647	767.5	35(15)	·	$(35/2^-)$
	x+4545	897.6	34(10)	·	·
Delayed	707	388.4	100(4)	$(15/2^-)$	$11/2^-$
	1425	718.0	112(6)	$(19/2^-)$	$(15/2^-)$
	1813	388.1	100(4)	$(21/2^+)$	$(19/2^-)$
	1981	168.1	53(2)	$(25/2^+)$	$(21/2^+)$
	2242	261.2	43(3)	$(27/2^+)$	$(25/2^+)$
	2421	178.9	18(2)	$(29/2^+)$	$(27/2^+)$
	2462	481.2	11(1)	$(29/2^+)$	$(25/2^+)$

TABLE II. The γ-ray transitions in ^{197}Au. The "x" denotes the unobserved low-energy transition from the $(31/2^-)$ state to the $(29/2^+)$ state.

	E_{level} (keV)	E_γ (keV)	$I_{\gamma+\mathrm{ce}}$	I_i	I_f
Prompt	767	357.9	100(8)	$(15/2^-)$	$11/2^-$
	1407	639.8	24(4)	$(19/2^-)$	$(15/2^-)$
	2097	260.9	58(3)	$(25/2^+)$	$(21/2^+)$
Prompt	x+2861	328.0	100(4)	$(35/2^-)$	$(31/2^-)$
	x+3410	549.4	78(3)	$(39/2^-)$	$(35/2^-)$
	x+4179	769.1	55(18)	$(43/2^-)$	$(39/2^-)$
	x+3876	465.2	28(2)	·	$(39/2^-)$
Delayed	767	357.9	100(7)	$(15/2^-)$	$11/2^-$
	1407	639.7	104(7)	$(19/2^-)$	$(15/2^-)$
	1836	429.1	107(7)	$(21/2^+)$	$(19/2^-)$
	2097	260.9	86(5)	$(25/2^+)$	$(21/2^+)$
	2533	435.5	93(6)	$(29/2^+)$	$(25/2^+)$

TABLE III. The γ-ray transitions in ^{199}Au. The "x" denotes the unobserved low-energy transition from the $(25/2^+)$ state to the $(21/2^+)$ state.

	E_{level} (keV)	E_γ (keV)	$I_{\gamma+\mathrm{ce}}$	I_i	I_f
Prompt	317	317.4	51(6)	$(5/2^+)$	$3/2^+$
	494	493.8	100(8)	$(7/2^+)$	$3/2^+$
Prompt	911	361.9	100(17)	$(15/2^-)$	$(11/2^-)$
	1505	594.4	79(21)	$(19/2^-)$	$(15/2^-)$
Prompt	x+2439	358.5	100(19)	$(29/2^+)$	$(25/2^+)$
	x+3037	597.7	52(18)	$(33/2^+)$	$(29/2^+)$
Delayed	494	493.9	100(5)	$(7/2^+)$	$3/2^+$
Delayed	911	361.5	100(9)	$(15/2^-)$	$(11/2^-)$
	1505	593.9	109(19)	$(19/2^-)$	$(15/2^-)$
	2080	574.3	46(11)	$(21/2^+)$	$(19/2^-)$

TABLE IV. The γ-ray transitions in ^{201}Au. The "x" denotes the unobserved low-energy transition from the $(25/2^+)$ state to the $(21/2^+)$ state.

	$E_{\rm level}$ (keV)	E_γ (keV)	$I_{\gamma+{\rm ce}}$	I_i	I_f
Prompt	973	378.6	100(14)	$(15/2^-)$	$11/2^-$
	1612	638.4	32(7)	$(19/2^-)$	$(15/2^-)$
Prompt	x+2554	362.7	100(6)	$(29/2^+)$	$(25/2^+)$
	x+3253	699.2	57(5)	$(33/2^+)$	$(29/2^+)$
Delayed	554	554.1	100(10)	$(7/2^+)$	$3/2^+$
Delayed	973	378.7	100(8)	$(15/2^-)$	$11/2^-$
	1612	637.9	109(11)	$(19/2^-)$	$(15/2^-)$
	2192	579.6	90(8)	$(21/2^+)$	$(19/2^-)$

TABLE V. The γ-ray transitions in ^{196}Au.

	$E_{\rm level}$ (keV)	E_γ (keV)	$I_{\gamma+{\rm ce}}$	I_i	I_f
Prompt	975	379.3	100(22)	(14^-)	12^-
	1680	705.5	66(14)	(16^-)	(14^-)
	2508	828	55(8)	(18^-)	(16^-)
	3020	511.6	55(2)	(20^-)	(18^-)
	3264	244	54(15)	(22^-)	(20^-)
	3656	392.4	45(8)	(24^-)	(22^-)
	1309	333.6	56(2)	·	(14^-)
	1923	614.6	27(2)	·	·

TABLE VI. The γ-ray transitions in ^{198}Au.

	$E_{\rm level}$ (keV)	E_γ (keV)	$I_{\gamma+{\rm ce}}$	I_i	I_f
Prompt	492	179.8	100(15)	(7^+)	5^+
	696	203.5	57(3)	(8^+)	(7^+)
Prompt	1105	292.8	100(2)	(14^-)	(12^-)
	1636	530.9	88(1)	(16^-)	(14^-)
	2383	746.8	56(2)	(18^-)	(16^-)
	2410	774.2	45(5)	·	(16^-)
	2769	386.1	37(6)	(18^+)	(18^-)
	3180	410.6	29(5)	(20^+)	(18^+)
	3172	403.1	12(3)	·	(18^+)
Delayed	215	215.0	100(6)	4^-	2^-
	312	97.4	92(5)	5^+	4^-

TABLE VII. The γ-ray transitions in ^{200}Au.

	$E_{\rm level}$ (keV)	E_γ (keV)	$I_{\gamma+{\rm ce}}$	I_i	I_f
Prompt	1343	333.1	100(6)	(14^-)	12^-
	1936	592.7	66(38)	(16^-)	(14^-)
	2701	764.7	49(8)	(18^-)	(16^-)
	2990	288.4	47(1)	(18^+)	(18^-)
	3212	221.9	25(1)	(20^+)	(18^+)
	3789	577.6	23(4)	(22^+)	(20^+)

TABLE VIII. The γ-ray transitions in ^{202}Au. The "x" denotes the level energy of the (12^-) state.

	$E_{\rm level}$ (keV)	E_γ (keV)	$I_{\gamma+{\rm ce}}$	I_i	I_f
Prompt	x+325	324.8	100(22)	(14^-)	(12^-)
	x+993	668.1	50(6)	(16^-)	(14^-)
	x+2040	1046.9	29(4)	(18^-)	(16^-)
	x+2475	435.4	28(5)	(18^+)	(18^-)

[1] Y. Cho, Y. Kim, A. Navin, et al., Physics Letters B 878 (2026) 140558. doi:https://doi.org/10.1016/j.physletb.2026.140558.

[2] G. Herling, T. Kuo, Nuclear Physics A 181 (1) (1972) 113–131. doi:https://doi.org/10.1016/0375-9474(72)90905-0.

[3] E. K. Warburton, B. A. Brown, Phys. Rev. C 43 (1991) 602–617. doi:10.1103/PhysRevC.43.602.

[4] C. Yuan, M. Liu, N. Shimizu, et al., Phys. Rev. C 106 (2022) 044314. doi:10.1103/PhysRevC.106.044314.

[5] S. J. Steer, Z. Podolyák, S. Pietri, et al., Phys. Rev. C 84 (2011) 044313. doi:10.1103/PhysRevC.84.044313.

[6] Z. Podolyák, G. Farrelly, P. Regan, et al., Physics Letters B 672 (2) (2009) 116–119. doi:https://doi.org/10.1016/j.physletb.2009.01.007.

[7] G. D. Dracoulis, Physica Scripta 2013 (T152) (2013) 014015. doi:10.1088/0031-8949/2013/T152/014015.

[8] E. M. Burbidge, G. R. Burbidge, W. A. Fowler, F. Hoyle, Rev. Mod. Phys. 29 (1957) 547–650. doi:10.1103/RevModPhys.29.547.

[9] M. Mumpower, R. Surman, G. McLaughlin, A. Aprahamian, Progress in Particle and Nuclear Physics 86 (2016) 86–126. doi:https://doi.org/10.1016/j.ppnp.2015.09.001.

[10] M. R. Mumpower, T. M. Sprouse, J. M. Miller, et al., The Astrophysical Journal 970 (2) (2024) 173. doi:10.3847/1538-4357/ad5afc.

[11] A. Kumar, N. Shimizu, Y. Utsuno, et al., Phys. Rev. C 109 (2024) 064319. doi:10.1103/PhysRevC.109.064319.

[12] T. Suzuki, T. Yoshida, T. Kajino, T. Otsuka, Phys. Rev. C 85 (2012) 015802. doi:10.1103/PhysRevC.85.015802.

[13] M. Venhart, J. L. Wood, M. Sedlák, et al., Journal of Physics G: Nuclear and Particle Physics 44 (7) (2017) 074003. doi:10.1088/1361-6471/aa7297.

[14] Y. Gono, R. Lieder, M. Müller-Veggian, et al., Physics Letters B 70 (2) (1977) 159–162. doi:https://doi.org/10.1016/0370-2693(77)90510-X.

[15] Y. Gono, R. Lieder, M. Müller-Veggian, et al., Nuclear Physics A 327 (2) (1979) 269–287. doi:https://doi.org/10.1016/0375-9474(79)90259-8.

[16] P. Tjøm, M. Maier, D. Benson, et al., Nuclear Physics A 231 (3) (1974) 397–410. doi:https://doi.org/10.1016/0375-9474(74)90504-1.

[17] V. Kölscbach, P. Schüler, K. Hardt, et al., Nuclear Physics A 439 (2) (1985) 189–206. doi:https://doi.org/10.1016/0375-9474(85)90427-0.

[18] A. Neskakis, R. Lieder, H. Beuscher, et al., Physics Letters B 80 (3) (1979) 194–197. doi:https://doi.org/10.1016/0370-2693(79)90196-5.

[19] A. Neskakis, R. Lieder, H. Beuscher, et al., Nuclear Physics A 390 (1) (1982) 53–69. doi:https://doi.org/10.1016/0375-9474(82)90606-6.

[20] D. Bucurescu, N. V. Zamfir, Phys. Rev. C 95 (2017) 014329. doi:10.1103/PhysRevC.95.014329.

[21] C. Guo-Jie, L. Yu-Xin, C. Hui, S. Hui-Chao, Chinese Physics Letters 23 (8) (2006) 2042. doi:10.1088/0256-307X/23/8/022.

[22] E. Gueorguieva, C. Schück, A. Minkova, et al., Phys. Rev. C 68 (2003) 054308. doi:10.1103/PhysRevC.68.054308.

[23] Y. Oktem, D. L. Balabanski, B. Akkus, et al., Phys. Rev. C 76 (2007) 044315. doi:10.1103/PhysRevC.76.044315.

[24] S. C. Wang, X. H. Zhou, Y. D. Fang, et al., Phys. Rev. C 85 (2012) 027301. doi:10.1103/PhysRevC.85.027301.

[25] E. Gueorguieva, C. Schück, A. Minkova, et al., Phys. Rev. C 69 (2004) 044320. doi:10.1103/PhysRevC.69.044320.

[26] Y. Oktem, D. L. Balabanski, B. Akkus, et al., Phys. Rev. C 86 (2012) 054305. doi:10.1103/PhysRevC.86.054305.

[27] B. S. Gao, X. H. Zhou, Y. D. Fang, et al., Phys. Rev. C 86 (2012) 054310. doi:10.1103/PhysRevC.86.054310.

[28] N. Fotiades, R. O. Nelson, M. Devlin, et al., Phys. Rev. C 71 (2005) 064314. doi:10.1103/PhysRevC.71.064314.

[29] H. Miyahara, Y. Ogata, N. Ishikawa, et al., Applied Radiation and Isotopes 60 (2) (2004) 289–294. doi:https://doi.org/10.1016/j.apradiso.2003.11.030.

[30] M. Munger, R. Peterson, Nuclear Physics A 303 (1) (1978) 199–216. doi:https://doi.org/10.1016/0375-9474(78)90051-9.

[31] E. Flynn, R. E. Brown, J. Sunier, et al., Physics Letters B 105 (2) (1981) 125–129. doi:https://doi.org/10.1016/0370-2693(81)91004-2.

[32] A. Wapstra, P. Goudsmit, J. Jansen, et al., Nuclear Physics A 93 (3) (1967) 527–544. doi:https://doi.org/10.1016/0375-9474(67)90305-3.

[33] J. C. Cunnane, P. J. Daly, Phys. Rev. C 6 (1972) 1407–1411. doi:10.1103/PhysRevC.6.1407.

[34] J. Cunnane, R. Hochel, S. Yates, P. Daly, Nuclear Physics A 196 (3) (1972) 593–604. doi:https://doi.org/10.1016/0375-9474(72)90795-6.

[35] M. Bowry, ISOLDE newsletter spring 2011, [Accessed 30-07-2025] (2011).

[36] A. Barzakh, A. Andreyev, D. Atanasov, et al., Nucl. Instrum. Methods Phys. Res. B 513 (2022) 26–32. doi:https://doi.org/10.1016/j.nimb.2021.12.011.

[37] Z. Podolyák, EPJ Web Conf. 279 (2023) 08001. doi:10.1051/epjconf/202327908001.

[38] C. H. Dasso, G. Pollarolo, A. Winther, Phys. Rev. Lett. 73 (1994) 1907–1910. doi:10.1103/PhysRevLett.73.1907.

[39] V. Zagrebaev, W. Greiner, Phys. Rev. Lett. 101 (2008) 122701. doi:10.1103/PhysRevLett.101.122701.

[40] Y. X. Watanabe, Y. H. Kim, S. C. Jeong, et al., Phys. Rev. Lett. 115 (2015) 172503. doi:10.1103/PhysRevLett.115.172503.

[41] J. S. Barrett, W. Loveland, R. Yanez, et al., Phys. Rev. C 91 (2015) 064615. doi:10.1103/PhysRevC.91.064615.

[42] V. V. Desai, W. Loveland, K. McCaleb, et al., Phys. Rev. C 99 (2019) 044604. doi:10.1103/PhysRevC.99.044604.

[43] J. F. C. Cocks, P. A. Butler, K. J. Cann, et al., Phys. Rev. Lett. 78 (1997) 2920–2923. doi:10.1103/PhysRevLett.78.2920.

[44] L. Kraus, A. Boucenna, I. Linck, et al., Phys. Rev. C 37 (1988) 2529–2539. doi:10.1103/PhysRevC.37.2529.

[45] M. Guidry, S. Juutinen, X. Liu, et al., Physics Letters B 163 (1) (1985) 79–83. doi:https://doi.org/10.1016/0370-2693(85)90196-0.

[46] H. Watanabe, Y. Watanabe, Y. Hirayama, et al., Physics Letters B 814 (2021) 136088. doi:https://doi.org/10.1016/j.physletb.2021.136088.

[47] Y. Hirayama, Y. X. Watanabe, M. Mukai, et al., Phys. Rev. C 98 (2018) 014321. doi:10.1103/PhysRevC.98.014321.

[48] P. R. John, J. J. Valiente-Dobón, D. Mengoni, et al., Phys. Rev. C 95 (2017) 064321. doi:10.1103/PhysRevC.95.064321.

[49] P. R. John, V. Modamio, J. J. Valiente-Dobón, et al., Phys. Rev. C 90 (2014) 021301. doi:10.1103/PhysRevC.90.021301.

[50] Y. Watanabe, Y. Hirayama, M. Mukai, et al., Nuclear Physics A 1061 (2025) 123140. doi:https://doi.org/10.1016/j.nuclphysa.2025.123140.

[51] Y. Hirayama, M. Mukai, Y. Watanabe, et al., Interactions 245 (1) (2024) 41. doi:10.1007/s10751-024-01886-1.

[52] Y. Hirayama, M. Mukai, Y. X. Watanabe, et al., Phys. Rev. C 106 (2022) 034326. doi:10.1103/PhysRevC.106.034326.

[53] H. Choi, Y. Hirayama, S. Choi, et al., Phys. Rev. C 102 (2020) 034309. doi:10.1103/PhysRevC.102.034309.

[54] C. Wheldon, J. J. Valiente-Dobón, P. H. Regan, et al., Phys. Rev. C 74 (2006) 027303. doi:10.1103/PhysRevC.74.027303.

[55] G. D. Dracoulis, G. J. Lane, H. Watanabe, et al., Phys. Rev. C 87 (2013) 014326. doi:10.1103/PhysRevC.87.014326.

[56] E806-20 Collaboration, E806-20 GANIL dataset (2021). doi:10.26143/GANIL-2021-E806_20.

[57] M. Rejmund, B. Lecornu, A. Navin, et al., Nucl. Instrum. Methods Phys. Res. A 646 (1) (2011) 184–191. doi:https://doi.org/10.1016/j.nima.2011.05.007.

[58] M. Vandebrouck, A. Lemasson, M. Rejmund, et al., Nucl. Instrum. Methods Phys. Res. A 812 (2016) 112–117. doi:https://doi.org/10.1016/j.nima.2015.12.040.

[59] A. Lemasson, M. Rejmund, Nucl. Instrum. Methods Phys. Res. A 1054 (2023) 168407. doi:https://doi.org/10.1016/j.nima.2023.168407.

[60] Y. Cho, Y. Kim, S. Choi, et al., Nucl. Instrum. Methods Phys. Res. B 541 (2023) 240–242. doi:https://doi.org/10.1016/j.nimb.2023.05.053.

[61] Y. Son, Y. Kim, Y. Cho, et al., Nucl. Instrum. Methods Phys. Res. B 540 (2023) 234–236. doi:https://doi.org/10.1016/j.nimb.2023.04.024.

[62] J. Simpson, F. Azaiez, G. de France, et al., Acta Physica Hungarica New Series-Heavy ion 11 (2000) 159–188.

[63] A. B. Brown, C. W. Snyder, W. A. Fowler, C. C. Lauritsen, Phys. Rev. 82 (1951) 159–181. doi:10.1103/PhysRev.82.159.

[64] S. Szilner, C. A. Ur, L. Corradi, et al., Phys. Rev. C 76 (2007) 024604. doi:10.1103/PhysRevC.76.024604.

[65] S. Akkoyun, A. Algora, B. Alikhani, et al., Nucl. Instrum. Methods Phys. Res. A 668 (2012) 26–58. doi:https://doi.org/10.1016/j.nima.2011.11.081.

[66] E. Clément, C. Michelagnoli, G. de France, et al., Nucl. Instrum. Methods Phys. Res. A 855 (2017) 1–12. doi:https://doi.org/10.1016/j.nima.2017.02.063.

[67] J. Dudouet, Cubix (1.3) (Dec. 2024). doi:10.5281/zenodo.15100409.

[68] ROOT: analyzing petabytes of data, scientifically. — root.cern, https://root.cern (2024).

[69] T. Kibédi, T. Burrows, M. Trzhaskovskaya, et al., Nucl. Instrum. Methods Phys. Res. A 589 (2) (2008) 202–229. doi:https://doi.org/10.1016/j.nima.2008.02.051.

[70] ENSDF database at National Nuclear Data Center, available at https://www.nndc.bnl.gov/ensdf/.

[71] J. Borggreen, R. Naumann, Nuclear Physics A 115 (1) (1968) 14–16. doi:https://doi.org/10.1016/0375-9474(68)90638-6.

[72] K. Okano, Y. Kawase, S. Uehara, T. Hayashi, Nuclear Physics A 136 (2) (1969) 321–336. doi:https://doi.org/10.1016/0375-9474(69)90057-8.

[73] K. J. Moody, N. Gharibyan, D. A. Shaughnessy, et al., Journal of Physics G: Nuclear and Particle Physics 47 (4) (2020) 045116. doi:10.1088/1361-6471/ab67e9.

[74] A. Metz, J. Jolie, G. Graw, et al., Phys. Rev. Lett. 83 (1999) 1542–1545. doi:10.1103/PhysRevLett.83.1542.

[75] J. A. Mirza, K. E. G. Löbner, D. Breitig, et al., Zeitschrift für Physik A Atoms and Nuclei 272 (2) (1975) 175–187. doi:10.1007/BF01408145.

[76] D. Negi, S. K. Tandel, P. Chauhan, et al., Phys. Rev. C 100 (2019) 014329. doi:10.1103/PhysRevC.100.014329.

[77] K. Sakai, P. Daly, Nuclear Physics A 118 (2) (1968) 361–368. doi:https://doi.org/10.1016/0375-9474(68)90342-4.

[78] J. C. Hill, D. G. Shirk, R. F. Petry, K. H. Wang, Phys. Rev. C 13 (1976) 2484–2491. doi:10.1103/PhysRevC.13.2484.

[79] S. Suman, S. K. Tandel, A. Kumawat, et al., Phys. Rev. C 103 (2021) 014319. doi:10.1103/PhysRevC.103.014319.

[80] N. Shimizu (2013). arXiv:1310.5431.

[81] J. Chen, M. Liu, C. Yuan, et al., Phys. Rev. C 107 (2023) 054306. doi:10.1103/PhysRevC.107.054306.

[82] S. Sahoo, P. C. Srivastava, N. Shimizu, Y. Utsuno, Phys. Rev. C 110 (2024) 024306. doi:10.1103/PhysRevC.110.024306.

[83] H. Toki, H. L. Yadav, A. Faessler, Zeitschrift für Physik A Atoms and Nuclei 292 (1) (1979) 79–94. doi:10.1007/BF01434634.